Hidden in Plain Sight: Examining Optically Selected Galaxy Clusters in the X-ray up to $z \sim 2$

Zoe Kearney, Department of Physics

Faculty of Science

McGill University, Montreal

June, 2023

A thesis submitted to McGill University in partial fulfillment of the requirements of the degree of

Master of Science

Table of Contents

Abstract

Selection bias among galaxy clusters is one of the most prevalent issues in observation, and with extensive galaxy cluster surveys on the horizon with implications for cosmological models, our understanding of these biases is crucial. We aim to continue to push the understanding of how the properties of galaxy clusters can result in evaded direct detection, specifically in the X-ray, as a function of redshift. Using the selected Spitzer Adaptation of the Red Sequence Cluster (SpARCS) survey, XMM-XXL X-ray cluster surveys, and *XMM-Newton* X-ray maps of the XMM-LSS field, W-CDF-S, and ELAIS-S1 fields, we examine the L_X vs. optical richness scaling relation at different redshifts for X-ray faint and bright clusters. We use the optically/IR-selected SpARCS cluster positions combined with stacking in the X-ray to explore the average properties of X-ray undetected clusters. Our stacking analysis allows us to incorporate a large range of properties in our cluster sample, specifically allowing us to push to low richnesses and higher redshifts ($z \sim 2$). We use principal component analysis to examine the homogeneity of the population of clusters going into our stacks and Bayesian linear regression to fit our scaling model.

Abrégé

Le biais de sélection parmi les amas de galaxies est l'un des problèmes les plus répandus en observation, et avec de vastes enquêtes sur les amas de galaxies à l'horizon avec des implications pour les modèles cosmologiques, notre compréhension de ces biais est cruciale. Nous visons à continuer à pousser la compréhension de la façon dont les propriétés des amas de galaxies peuvent entraîner une détection directe éludée, en particulier dans les rayons X, en fonction de redshift. À l'aide de Spitzer Adaptation of the Red Sequence Cluster (SpARCS), des études XMM-XXL X-ray cluster, et des cartes de rayonnement *XMM-Newton* du champ XMM-LSS, W-CDF-S et ELAIS-Champs S1, nous examinons la relation de mise à l'échelle L_X par rapport à la richesse optique à différents redshifts pour les faisceaux de rayons X faibles et brillants. Nous utilisons les positions de amas SpARCS sélectionnées optiquement/IR combinées à l'empilage dans les rayons X pour explorer les propriétés moyennes des amas non détectées dans les rayons X. Notre analyse de cumul nous permet d'intégrer une large gamme de propriétés dans notre échantillon de amas, ce qui nous permet de pousser vers des richesses inférieures et des redshifts plus élevés ($z \sim 2$). Nous utilisons l'analyse des composantes principales pour exam-

iner l'homogénéité de la population de amas entrant dans notre empilage et la régression linéaire bayésienne pour adapter notre modèle d'échelle.

Acknowledgements

I would like to thank everyone who supported me throughout my Master's, in Montreal and elsewhere. Thank you Tracy for giving me the room and support to grow as a researcher, thank you to fellow students at the TSI who kept me sane, thank you to my dear friends Nicole and Bailey for getting me through grad school, thank you to my partner Zach for being an incredible supporter, and thank you to my friends and family around the world for cheering me on.

Contribution of Authors

Zoe Kearney completed all chapters with input and guidence from her advisor, Professor Tracy Webb, especially in the discussion section. Professor Adrian Liu aided with data methods and interpretation, especially in section 3.3.1. Dr. Kristen Dage aided in suggesting additional X-ray detection methods (section 3.3.1). Graduate student Soumya Shreeram aided with discussion surrounding stacking methods (section 3.2.2).

List of Figures

List of Tables

Abbreviations

Abbreviation	Meaning
ΛCDM	Lambda cold dark matter
H_0	Hubble constant
Ω_0	mass density
ICM	intracluster medium
SZ	Sunyaev-Zeld'ovich
CMB	cosmic microwave background
eROSITA	extended ROentgen Survey with an Imaging Telescope Array
CRS	cluster red sequence method
SpARCS	Spitzer Adaptation of the Red-sequence Custer Survey
BCG	Brightest Cluster Galaxy
R_{500}	Radius of volume with mass density 500 times average density of the universe
$M^*_{3.6\mu m}$	Knee of the absolute magnitude function
NED	NASA extragalactic database
PCA	principal component analysis
EOF	empirical orthogonal functions
PC	principal component
p-n	*XMM-Newton* detector
MOS	metal oxide semiconductor, *XMM-Newton* detector
ECF	energy conversion factor
PSF	point spread function
R-hat	potential scale reduction factor
Mpc	megaparsecs
kpc	kiloparsecs
L_X	X-ray luminosity
keV	kiloelectron volts
KDE	kernal density estimation

Chapter 1

Introduction

One of the largest challenges when studying galaxy clusters is studying the populations at $z > 1$. This analysis is even more difficult when comparing observational selection methods and examining the biases that they induce in cluster surveys and scaling relations. However, understanding these biases at high z is becoming increasingly important as next-generation X-ray instruments become available and unparalleled numbers of galaxy clusters are identified. There are several unanswered questions in the field, such as how do observational biases affect certain scaling relations at high redshift? Are X-ray faint galaxy clusters represented in selection models? Do galaxy clusters' ability to turn gas into stellar mass change over time? This work aims to contribute to these questions using various analysis methods.

The main objectives of this thesis are as follows. Use stacking analysis to examine the average X-ray properties of galaxy clusters detected in the optical and infrared but not individually detected in the X-ray. Examine where this cluster population resides on the X-ray luminosity vs. optical richness (L_X-Ngal) scaling relation, especially compared to

clusters that are detectable in the X-ray and the optical. Identify the presence or lack of observational bias in the L_X-Ngal relation when clusters are selected with optical methods versus with X-ray and compare findings with literature. Examine the evolution of the L_X-Ngal up to $z \sim 2$ and compare with previous findings of its evolution up to $z \sim 0.3$ (Rykoff et al. (2008)).

This thesis is laid out as follows. In Chapter 2, the relevant literature in the field is summarized. Chapter 3 includes the selection process of the optical/infrared and X-ray data, methods used for stacking analysis, principal component analysis, bootstrapping, and our results for the L_X- Ngal relation. Section 4 includes a discussion of findings, compares results with those found in the literature, addresses caveats, and indicates the next steps for this research. Section 5 includes an overall summary. We assume a flat ΛCDM cosmology with H_0=67.77 km/sec/Mpc and Ω_0=0.307115 (Soumya Shreeram, private correspondence).

Chapter 2

Literature Review

2.1 Background

2.1.1 Galaxy clusters

Galaxy clusters are the largest virialized structures in the universe. A key application of galaxy clusters is their prevalence in cosmological models (Kaiser (1986), Böhringer et al. (2004), Henry et al. (2009), De Martino and Atrio-Barandela (2016b), Migkas et al. (2021)). From the dark matter detections in 1933 to using the brightest cluster galaxy as standard candles, clusters have historically been fundamental to understanding dark matter, structure formation, and evolution (Allen et al. (2011)). When clusters are assumed to form from spherically symmetric mass perturbations, their growth is an ideal proxy for understanding the evolution of dark matter and energy in the universe (Kaiser (1986), Voit (2005)). Large-scale evolution can also be examined by studying the properties of clusters at different epochs (Voit, 2005). In addition to cosmological applications, the highly dense

and gravitational bound populations of galaxies in a cluster provide contrast to galaxies residing in the field. This contrast allows for the study of environmental influence on galaxies which has been shown to have had impacts on galaxy formation models (Peng et al. (2010), Scoville et al. (2013)).

Many techniques and wavelengths are used to detect and measure the properties of galaxy clusters. X-ray observations probe the extremely hot and ionized intracluster medium (ICM) and AGN activity while optical traces the overdensities of cluster members (Byram et al. (1966), Abell et al. (1989), Dalton et al. (1997), Scharf et al. (1997), Borgani et al. (2002)). The Sunyaev-Zeld'ovich (SZ) effect measures the distortion of the cosmic microwave background (CMB) spectrum after passing through clusters and receiving a boost of energy due to inverse-compton scattering (Sunyaev and Zeldovich (1972)). The different observational techniques probe varying physical processes occurring within clusters and their evolution as a population (Giodini et al. (2013)). It is, therefore, imperative to understand how the different properties of clusters are related, not only to discern the physics of cluster formation and evolution but to calibrate cosmological models.

2.1.2 Scaling relations

Scaling relations are one of the most essential tools for exploring the connections between properties of clusters observed at different wavelengths and for measuring non-observable quantities such as cluster mass (Giodini et al. (2013)). Galaxy cluster scaling relations have been studied since the early 1970s (Mitchell et al. (1977)). Their scatter and disagreements with theory can also tell us more about the thermodynamic histories of

clusters as the physical processes that occur within these structures make them a prime laboratory for studying high energy physics (Morandi et al. (2007), De Martino and Atrio-Barandela (2016a), Giodini et al. (2013)). A historical assumption that is often made of galaxy clusters is that they follow self-similarity, which assumes that the primary source of thermal energy of the ICM is the gravitational energy lost due to the gravitational potential well of the cluster (Kaiser (1986), Molendi (2004)). Because this relationship can probe the nature of dark matter halos, and since dark matter follows self-similarity, relatively simple relationships can be established between cluster properties such as mass, luminosity, and temperature (Kaiser (1986)). The evolution at different redshifts in the self-similar model can also be captured using the mean and critical density of the universe (Kaiser (1986), Böhringer et al. (2012)). Tensions between self-similar model predictions and observations have furthered our knowledge of cluster physics, such as the presence of non-gravitational heating sources (Borgani et al. (2002)). Departure from theory has also been shown to significantly impact cosmological parameters, such as H_0 (Migkas et al. (2021)). Therefore, observational scaling relations must continue to be examined against theory, especially as a function of z.

2.2 Application

2.2.1 Clusters in the X-ray

The extremely hot and ionized plasma of the intracluster medium (ICM) of clusters has long been used to detect and measure galaxy clusters (Mitchell et al. (1977)). The bremsstrahlung

emission from accelerated free electrons in the gas can directly trace properties such as gas temperature, mass, and the nature of the dark matter halos in which clusters reside. It has previously been a challenge to extend cluster analysis to $z > 1$ because X-ray luminous clusters are rare at these redshifts (Henry et al. (1992), Rosati et al. (2002)). While data from the extended ROentgen Survey with an Imaging Telescope Array (eROSITA) is pushing to extend X-ray detection $z > 1$, this data has only become available in the last year, and the current surveys do not include enough passes to contain large numbers of clusters at these higher redshifts (Li et al. (2023)). Therefore, it was and remains pertinent to use additional detection methods to supplement the redshift and mass-limited X-ray data.

2.2.2 Clusters in the Optical and Infrared

Since the early 2000s, optical detection of clusters using the cluster-red-sequence method (CRS) and infrared coverage have become powerful tools for finding clusters, especially at higher redshift (Gladders and Yee (2000), Gladders and Yee (2005), Wilson et al. (2009), Muzzin et al. (2009)). As proposed by Gladders and Yee (2000), the CRS selection technique relies on the fact that all rich clusters have a population of early-type, elliptical galaxies.

These "red-sequence" populations not only have low scatter on a color-magnitude relation but they are also formed at higher redshifts making their evolution particularly homogeneous for clusters $z < 2$ (Bower et al. (1992),Gladders and Yee (2000)). With red-sequence populations being a unanimous signature within and between clusters, identi-

fying the over-densities of the populations is a powerful way to detect clusters and accurately measure their photometric redshifts (Gladders and Yee (2000)). CRS and other detection algorithms use the intrinsic signature of the 4000Å break to trace the old stellar population (Poggianti and Barbaro (1997), Gal et al. (2000)). However, unlike other cluster selection algorithms, the CRS aims to select clusters in a way that reduces the presence of projection effects, and uses only two color filters to sample the 4000Å break (Gladders and Yee (2000)). The red-sequence cluster survey (RCS), the first to exploit CRS, used the two optical filters R_c (centered at $\sim$ 6500Å) and z' (centered at $\sim$ 9100Å) to identify 67 cluster candidates over a redshift of $0.9 < z < 1.4$ (Gladders and Yee (2005)). While the RCS was able to examine clusters at $z \sim 1$, to push to even higher redshifts and adequately cover the 4000Å break, infrared (IR) data is necessary.

Spitzer fields provided sufficient deep and wide IR coverage to supplement the optical and X-ray data. The 3.6 μm IRAC band provided the red filter to span the 4000Å break at higher redshifts (Wilson et al. (2009), Muzzin et al. (2009)). Initially, the Spitzer first look survey (FLS) found 99 cluster candidates with the adapted CRS technique spanning $0.1 < z < 1.3$ (Muzzin et al. (2008)). However, Spitzer 3.6 μm data from the even deeper SWIRE Legacy fields combined with ground-based z' imaging filter pushed the redshift of cluster detection $z > 1.6$ in the Spitzer Adaptation of the Red-sequence Custer Survey (SpARCS) (Muzzin et al. (2009), Wilson et al. (2009)). The SpARCS -South cluster survey, with an area of 13.6 deg^2, utilizes observations from CTIO/MOSAICII and covers the ELAIS-S1 and Chandra-S SWIRE fields (Wilson et al. (2009)). The SpARCS - North cluster survey with an area of 28.3 deg^2 covers the ELAIS-N1, ELAIS-N2, XMM-LSS, and Lockman-Hole fields using data from CFHT (Muzzin et al. (2009)).

2.2.3 Brightest Cluster Galaxies

One challenge in the optical/IR selection of galaxy clusters is defining the position of the cluster. In the X-ray, the center is easily identified by the X-ray peak, which accurately traces the bottom of the cluster's gravitational potential. However, in the optical, the position can be defined as either the red-sequence center, which occurs at the color peak in the red filter, or the brightest cluster galaxy (BCG). The BCG is the preferred position because red-sequence centers are often poorly defined and do not always correlate with a single galaxy in the cluster (Willis et al. (2018)). For the SpARCS catalog, BCGs are identified by selecting the brightest galaxy in the 3.6 μm channel with a color within $\pm$0.5 mag of the red sequence, which is predicted using the z'-3.6 μm as previously discussed (Muzzin et al. (2009),Webb et al. (2015)).

However, there are caveats to the detection and use of BCGs as an accurate cluster position. One such bias is that the SpARCS BCG identification is preferential towards BCGs with colors consistent with the red sequence, which can result in the omission of BCGs that are undergoing star formation or are obscured by dust (Webb et al. (2015)). Another concern is the potential offset between the well-defined X-ray emission peak and the BCG. This offset has been shown to be, overall, negligible for relaxed clusters indicating that the BCG is a good proxy for the cluster center (Jones and Forman (1984), Lin and Mohr (2004), Lin et al. (2017), Lopes et al. (2018)). However, at higher redshifts, cluster morphology can be less homogeneous, and clusters may not be in equilibrium leading to higher offsets ($> 0.01 \times R_{500}$) between the X-ray centroid and the BCG (Webb

et al. (2015), Willis et al. (2018), Lopes et al. (2018)). The potential implications of these biases will be addressed in the discussion section.

2.2.4 Observational Biases

While detecting clusters with different observational techniques can be complementary, there are limitations for every method. These limitations have been shown to introduce non-negligible bias to cluster surveys and, therefore, to scaling relations (Rykoff et al. (2008), Willis et al. (2018)). X-ray surveys are typically flux-limited, which impacts studying scaling relations at different redshifts and causes bias towards X-ray bright clusters which can depend on cluster morphology (Böhringer et al. (2004), Willis et al. (2018)). Selection effects are well studied at low redshift ($z < 0.3$) but are lacking at higher redshifts due to limited large area surveys and sample sizes (Rozo et al. (2014), Willis et al. (2018)).

An initial examination of the XMM-LSS field SpARCS clusters in the X-ray is conducted by Willis et al. (2018), however, using relatively shallow XMM-LSS X-ray field data. A key result of this study is tentative evidence that the red-sequence population in X-ray selected clusters is smaller than the red-sequence population in optically selected clusters, even if the clusters are X-ray bright (Willis et al. (2018)). They also find larger offsets in the BCG- barycentre positions for clusters that are X-ray faint but bright in the optical, indicating that these clusters may represent a population of clusters that recently underwent a merger or another dynamic disturbance (Willis et al. (2018)). As X-ray faint clusters are much less likely to be detected by X-ray selection methods, this implies that X-ray cluster surveys may also be biased against systems that are not in equilibrium. This

study, along with others, highlights the importance of furthering our understanding of X-ray faint cluster populations and their inclusion in cluster selection functions and scaling relation models (Lopes et al. (2006), Rossetti et al. (2017), Willis et al. (2018)).

2.2.5 The L_X- Richness relation

Many scaling relations and their associated observational biases have been studied over the last 30 years. However, many relations and how the physical properties of cluster samples depend on observational methods, still need to be an examined above $z \sim 1$ (Willis et al. (2018)). Looking at scaling relations between two observables to avoid inducing additional errors is especially meaningful. Variations of the L_X-Ngal relation have been reasonably well examined at $z < 0.4$ using direct observables for both L_X and optical richness (Gilbank et al. (2004), Lopes et al. (2006), Dai et al. (2007), Rykoff et al. (2008), Gal et al. (2009)). This relation and similar proxies contain information about cluster morphology, substructure, and the X-ray luminosity function of clusters (Lopes et al. (2006), Rykoff et al. (2008), Willis et al. (2018), Popesso et al. (2023)). The biases present in the L_X-richness relation are especially important to identify and constrain as this relation also contains intrinsic scatter due to the Poisson scatter in richness (Lopes et al. (2006), Rettura et al. (2018)).

Examining two observables is an ideal time to investigate the presence of selection effects. Rykoff et al. (2008) examines the L_X- Richness relation between clusters that were selected in the X-ray versus the optical from $0.1 < z < 0.3$ using the optically selected maxBCG catalog. While they use X-ray data from sources matched to their maxBCG sam-

ple instead of direct X-ray properties of the optical sources, their strict matching criteria allow for meaningful comparisons. Even though their X-ray-selected clusters have X-ray luminosities below what they would expect, they are still higher at a given richness than the optically selected clusters (Rykoff et al. (2008)). This is relatively unsurprising since the X-ray selection should pick out the most X-ray bright clusters yet is still meaningful, especially at low z where, due to evolution, clusters are less X-ray luminous (Rykoff et al. (2008), Kaiser (1986)).

Another natural progression is to examine the evolution of the relation as a function of z. Although they are restricted by the relative local redshift span, Rykoff et al. (2008) also examines this. They find the optically selected higher redshift clusters are significantly more luminous than the lower redshift optically selected clusters (Rykoff et al., 2008). While this result is generally expected due to self-similarity, they note that the difference is more extensive than expected (Kaiser (1986), Rykoff et al. (2008)). This difference is partly due to the poor understanding of the redshift evolution of optical richness when measured with a scaled aperture (Rettura et al. (2018)). To further understand how this relation evolves and if selection effects impact that evolution, we must push above $z \sim 0.4$. Since the peak of global star formation occurred at $z \sim 2$, pushing a scaling relation such as L_X- richness to these redshifts means we are probing cluster evolution over epochs crucial to large-scale structure formation and examining galaxy cluster efficiency over time (Madau and Dickinson (2014)).

Chapter 3

Body

3.1 Data

3.1.1 SpARCS Cluster Selection

Our main sample is comprised of clusters that are optically/FIR selected from the SpARCS catalog. This catalog includes 1343 clusters from the XMM-LSS, W-CDF-S, and ELAIS-S1 fields. The XMM-LSS field is centered on (02:21:20 RA, -04:30:00 DEC) with a SWIRE 3.6 μm (”red” filter) coverage area of 9.4 deg^2, and a z' band (”blue” filer) coverage area of 11.7 deg^2 (Wilson et al. (2009)). The W-CDF-S field is centered on (03:32:00 RA, -28:16:00 DEC) with a SWIRE 3.6 μm coverage area of 8.1 deg^2, and a z' band coverage area of 7.9 deg^2 (Wilson et al. (2009)). The ELAIS-S1 field is centered on (00:38:30 RA,-44:00:00 DEC) with a SWIRE 3.6 μm coverage area of 7.1 deg^2, a z' band coverage area of 8.3 deg^2 (Wilson et al. (2009)).

Unless otherwise specified, the SpARCS positions used and referenced herein is coordinates of the BCG as detected using the methods described in section 2.2.3. All SpARCS clusters are assigned an optical richness measurement (herein referred to as Ngal). Ngal is defined as the number of background-subtracted galaxies within an aperture of 500 kpcs above a limit of $M^*_{3.6\mu m} + 1$ (Webb et al. (2015)). We limit our sample to clusters with Ngal > 0, as all other clusters are assumed to be non-physical. While other analyses done using the SpARCS catalog use a slightly higher Ngal cut of 5 or 10 (Willis et al. (2018)), we choose to leave in the low richness clusters due to our stacking analysis and the aim to push to lower richnesses. The richnesses and redshifts covered by our sample for each field are represented in figure 3.1. We note that the expected slight increase in richness at higher redshifts is observed in each field due to selection effects.

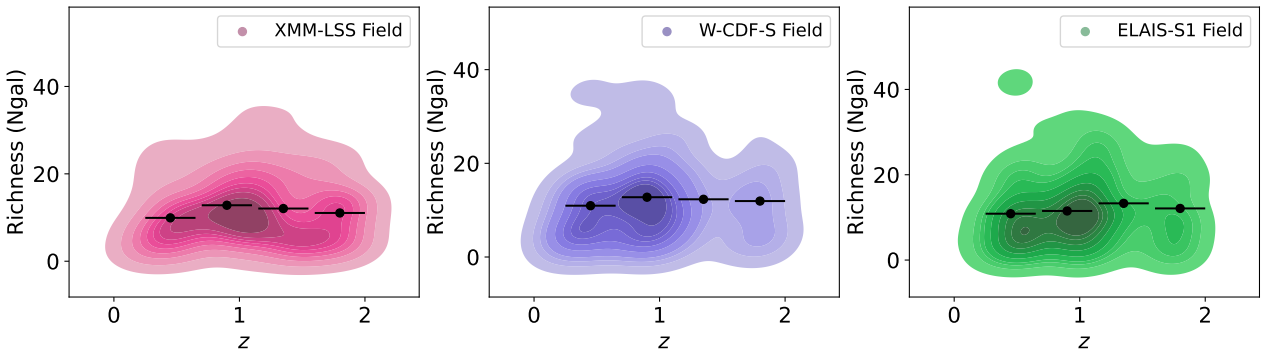

Figure 3.1: Distribution of clusters in richness vs. redshift space for each field, created using kernel density estimation (Waskom (2021)). Binned averages are shown in black scatter points to demonstrate the slight increase in richness at higher redshifts. Errors on the redshifts show bin sizes and errors in richness are Poisson errors. Richness error bars are small compared to marker size.

To first order, local galaxy clusters have similar angular diameter distances. However, our SpARCS sample probes a range of redshifts that cover a significant range of angular

diameter distances. For the purposes of conducting stacking analysis in physical space and examining redshift evolution, we chose to put our cluster sample into redshift bins. Bounds on the redshift bins were chosen to maximize and equalize the number of clusters in each bin while minimizing the spread of the angular diameter distances. The redshift bins and the number of SpARCS clusters in each are summarized in table 3.1. We also show our sample's angular diameter distance distribution as a function of redshift in figure 3.2 for our given cosmology.

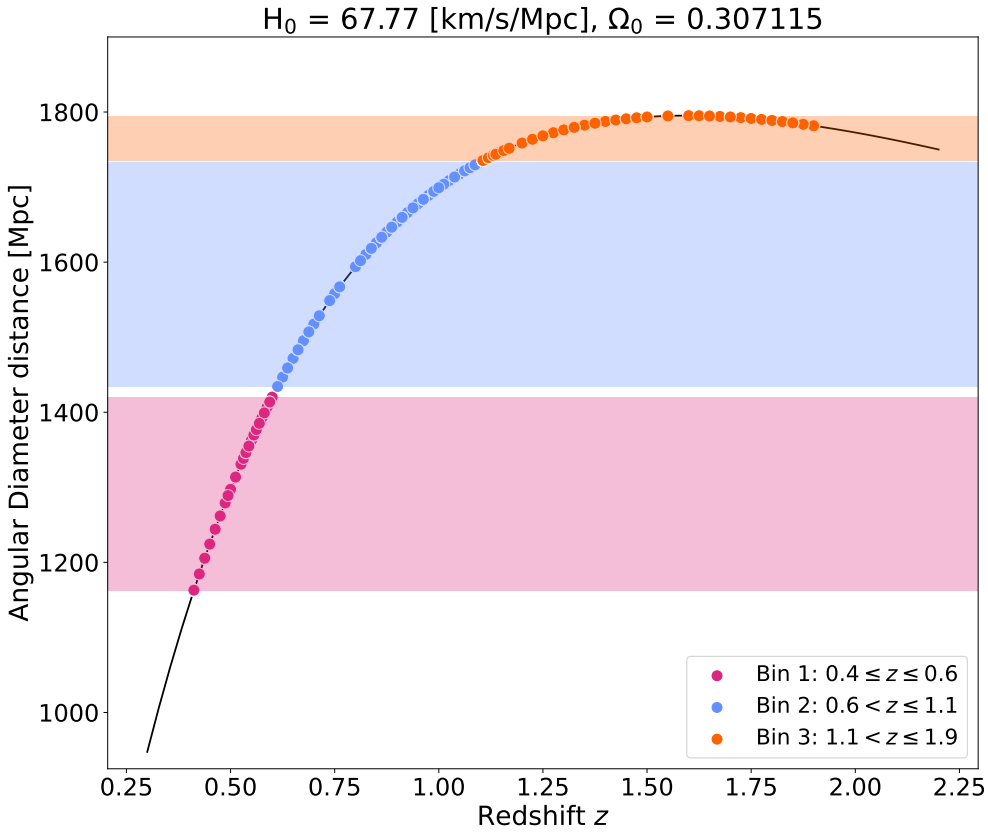

Figure 3.2: Angular diameter distance as a function of redshift for all SpARCS clusters in our sample. Each redshift bin is highlighted.

Table 3.1: Summary of redshift bin bounds and the number of SpARCS clusters included in each bin.

z bin	Number of SpARCS clusters
1 $(0.4 \leq z \leq 0.6)$	103
2 $(0.6 < z \leq 1.1)$	198
3 $(1.1 < z \leq 1.9)$	172

3.1.2 X-ray Field and Source Catalogs

Instead of using the properties from an X-ray clusters survey matched to our SpARCS sample to obtain a L_X measurement for each cluster, we directly analyze X-ray data. We obtain X-ray image data for our optically selected sample from two surveys conducted in the three fields of interest with data from *XMM-Newton*. We use Chen et al. (2018)'s medium deep X-ray survey, including their 5242 X-ray detected point source catalog, over a 5.3 deg^2 area in the XMM-LSS region. Chen et al. (2018) uses 1.3 Ms of new *XMM-Newton* observations and archival data to create uniform X-ray count, background, and exposure maps. The maps used in this analysis are in the soft band with an energy band of 0.5 - 2 keV and a flux limit of 1.7×10^{-15} erg/cm^2/s (Chen et al. (2018)). In addition to the image maps, the extensive point source catalog from Chen et al. (2018) is used to identify contaminating point sources and potentially misclassified point sources. The rectangular point source region is centered on RA = 35.580° and DEC = -4.965° and has a depth of 46 ks. Source detection was done using the SCIENCE ANALYSIS SOFTWARE (SAS) tasks EVWAVELET and ELMDETECT. SAS is the primary analysis software used to process the data taken with the instruments on *XMM-Newton*. The EVWAVELET task detects sources using the "Mexican hat" wavelet algorithm and the ELMDETECT task fits maximum like-

lihood multi-source point spread functions. Chen et al. (2018)'s spurious source detection is $\leq 1\%$ and 93% of the X-ray sources have a reliable optical- to-near-IR counterpart from the SERVS, VIDEO, CFHTLS, and HSC-SSP catalogs.

A similarly conducted survey was done in 2021 by Ni et al. (2021) covering the W-CDF-S and ELAIS-S1 fields. Again, using new *XMM-Newton* data combined with archival *XMM-Newton* and *Chandra* data, Ni et al. (2021) creates relatively uniform X-ray count, exposure, and background maps. The 4053 W-CDF-S point source catalog covers an area of 4.6 deg^2, with a depth of 84 ks and a soft band flux limit of 1.0×10^{-14} erg/cm^2/s. The 2630 ELAIS-S1 point source catalog covers an area of 3.2 deg^2, with a depth of 80 ks and a soft band flux limit of 1.3×10^{-14} erg/cm^2/s. Detection, counterpart identification, and redshift confirmation were done similarly to Chen et al. (2018).

Both sets of catalogs conduct AGN classification using optical counterpart color cut-offs and spectra when available (see Chen et al. (2018) and Ni et al. (2021) for additional details on this analysis). AGN classification is important for this analysis, as it allows for easy identification of sources with X-ray emission dominated by ICM emission as opposed to AGNs. The catalogs also only include sources without extended X-ray emission, as defined by ELMDETECT extended source flag. While the ELAIS-S1 and W-CDF-S X-ray point source catalogs have extensive coverage over their prospective fields, the XMM-LSS point sources are concentrated in a rectangular area in the center of the field (Chen et al. (2018), Ni et al. (2021)). We thus further restrict our optically selected sample to SpARCS clusters with positions within the X-ray point source coverage for each field. The X-ray maps from Ni et al. (2021) and Chen et al. (2018) overlaid with the spatial distribution of the SpARCS clusters included in our sample are shown in figure 3.3.

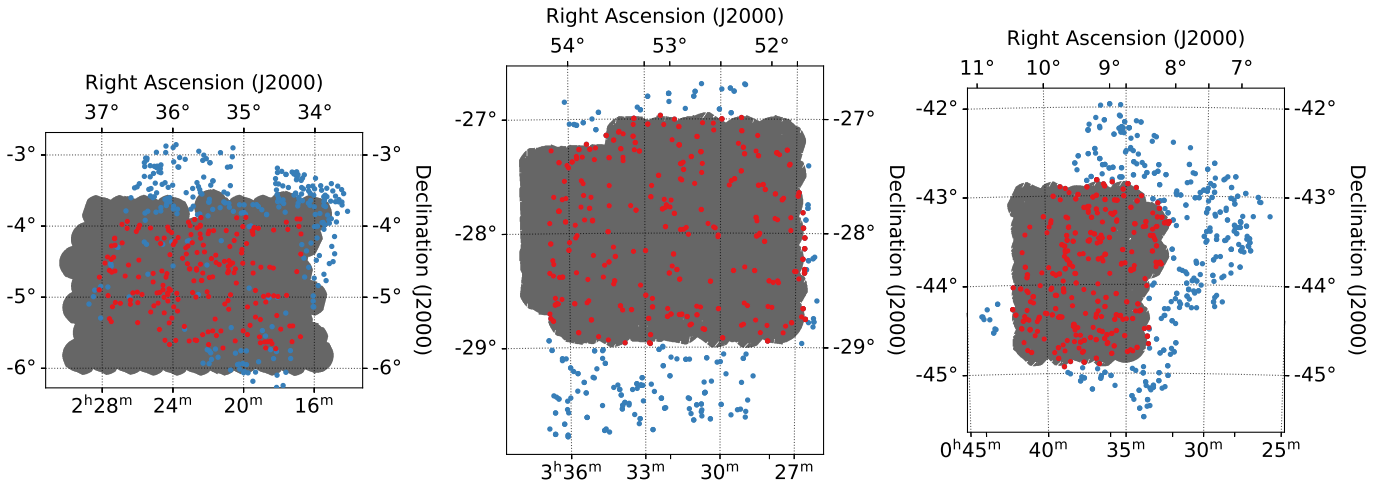

Figure 3.3: *Left*: X-ray coverage (grey) of the XMM-LSS field from Chen et al. (2018). Red points are SpARCS clusters included in our sample, blue points are SpARCS clusters with positions outside of the X-ray point source coverage. *Middle*: X-ray coverage (grey) of the W-CDF-S field from Ni et al. (2021). Red points are SpARCS clusters included in our sample, blue points are SpARCS clusters with positions outside of the X-ray point source coverage. *Right*: X-ray coverage (grey) of the ELAIS-S1 field from Ni et al. (2021). Red points are SpARCS clusters included in our sample.

In addition to the X-ray point sources in the three fields, we identify any confirmed X-ray detected clusters. We obtained 302 X-ray-detected clusters in the XMM-LSS field from the pubic XMM-XXL survey (Chiappetti et al. (2018)). As there is no X-ray detected cluster catalog for the W-CDF-S and ELAIS-S1 fields, we relied on an object search in NASA Extragalactic Database (NED) for X-ray observed clusters. Only two relevant X-ray clusters were found in the W-CDF-S and ELAIS-S1 fields.

3.2 Methods

3.2.1 Source Matching

Many of the SpARCS clusters have a counterpart in the X-ray. We expect this, especially of the SpARCS clusters that are bright in the X-ray (Anderson et al. (2015)). However, since we are exploring observational biases between detection methods, it is crucial to identify which SpARCS clusters are only detected using optical methods and which are detected with optical and X-ray. We, therefore, create two sub-samples in each redshift bin of our selected SpARCS clusters; the first is comprised of the clusters that have a counterpart in the X-ray (furthermore referred to as DXsC), and the second is comprised of the clusters that do not have a counterpart in the X-ray (furthermore referred to as UXsC). For a cluster to be in the DXsC sub-sample, we require that the cluster position either match with a confirmed X-ray detected cluster or with an X-ray point source.

We define a source match between a SpARCS cluster and a confirmed X-ray cluster as being within a radius of 120″. This radius was chosen to maximize accurate matches, which we confirm by comparing redshifts, but avoid spurious associations. We define a source match between a SpARCS cluster and an X-ray point source as being within a radius of 25″. The SpARCS clusters that are matched with a point source are characterized as an X-ray detected cluster because it has been shown that many X-ray point sources are misclassified clusters, especially when the cluster is compact and the point source function (PSF) of the X-ray instrument is large (Bulbul et al. (2021)). The 25″ search radii were chosen to ensure association and reduce the possibility of spurious matches along the line of sight. To further quantify this, we conduct a random matching experiment to

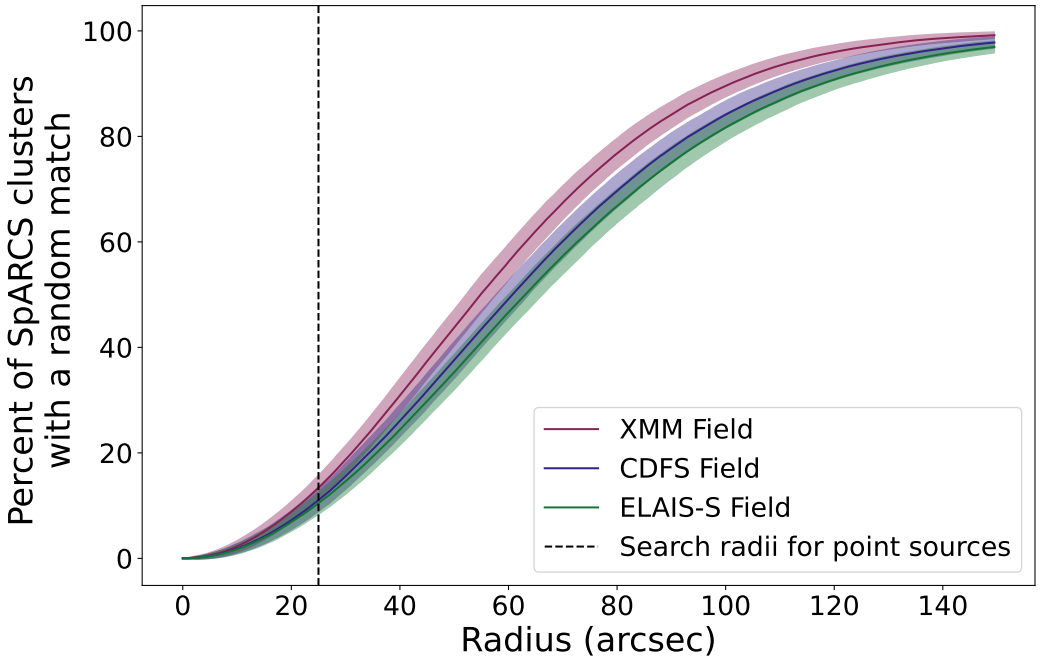

Figure 3.4: Probability of a spurious match with a SpARCS cluster in each field as a function of search radii. Solid line represents the mean percentage and shaded area represents 1σ error.

explore the number of SpARCS clusters matched with randomly placed positions within the field as a function of search radii. As shown in figure 3.4, less than 20% of our matches are spurious in all fields. We take the population of spurious matches into account later in the analysis.

During our analysis, we often see multiple SpARCS clusters matched to the same X-ray source or vice-versa. Our matching is fully comprehensive and classifies any SpARCS cluster within the search radii of at least one source as a member of the sub-sample DXsC. Table 3.2 summarizes the sub-sample numbers in each redshift bin.

Table 3.2: Summary of the SpARCS clusters included in each sub-sample of each z bin.

z bin	Number of clusters in DXsC	Number of clusters in UXsC
1 $(0.4 \leq z \leq 0.6)$	41	62
2 $(0.6 < z \leq 1.1)$	52	146
3 $(1.1 < z \leq 1.9)$	45	127

3.2.2 Stacking

Following separating the SpARCS cluster sample into clusters that were previously detected in the X-ray and clusters only detected in the optical/IR, we aim to directly measure the X-ray luminosity of clusters in both sub-samples and all z-bins to examine their location on our L_X-Ngal relation. The SpARCS clusters in the DXsC sub-sample are often bright in the X-ray resulting in their independent X-ray luminosity being easily measurable. However, many of the SpARCS clusters in the UXsC sub-sample are X-ray faint, and we cannot directly measure their X-ray luminosity. Therefore, we turn to stacking, a technique especially useful in the X-ray where increased exposure time is linearly related to the number of photons detected. By stacking, we can increase the individual exposure times on average from 10^4 to 10^7 seconds. We can then evaluate the stack's properties as an average of the stack members.

Using the X-ray counts, background, and exposure maps described in section 3.1.2, we first create masks to remove all point sources from each of the three fields. The creation of the masks is done by cutting out 68 arcsec regions around each X-ray point source, setting the pixels in the masked region to 0, and setting all other pixels to 1. 68" is chosen as a region size to mask the average size of the point sources. Three masks are made; an example of the mask made for the XMM-LSS field is shown in figure 3.5.

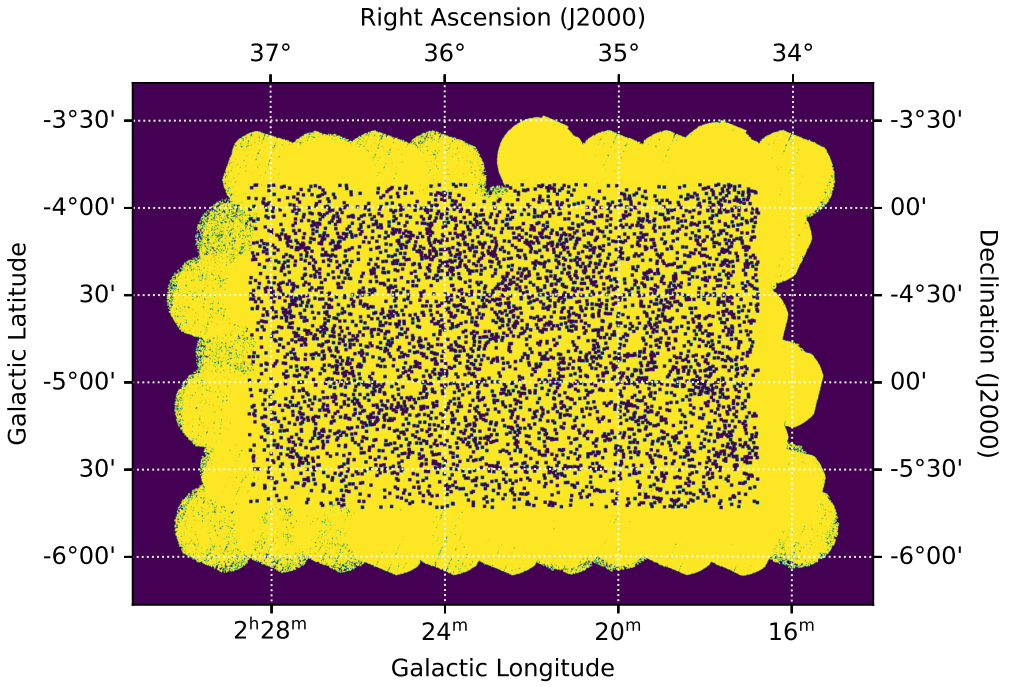

Figure 3.5: One of three whole field masks used to eliminate the X-ray detected point sources that lie outside a 25″ radius from of the SpARCS clusters selected for stacking analysis. This mask is for the XMM-LSS field. Purple represents a value of 0, yellow a value of 1, and any additional colors are functions of the image.

Stacking is conducted by creating a 2D cutout of the counts, background, exposure, and mask maps centered on the SpARCS position of the clusters in the UXsC sub-sample. All cutouts preserve the original image scale of 4″/pixel. The size of each cutout is 2 Mpc $\times$ 2 Mpc, with the physical to image scale conversion done using the average redshift of each z bin. The dimensions of the z bin 1, z bin 2, and z bin 3 stacks are (316″ $\times$ 316″), (248″ $\times$ 248″), and (228″ $\times$ 228″) respectively. Each cutout's pixels associated with a zero-value pixel in the mask are filled with random Poisson noise from smoothed ($\sigma = 25$) surrounding counts (Soumya Shreeram, private correspondence). This process ensures that the X-ray point sources do not contaminate the stacks and are instead modeled as background noise.

We correct each exposure cutout by a redshift dimming factor, ϕ, by using the equation

$$\phi = \frac{(1+z)^4}{(1+z_{\rm ref})^4} \tag{3.1}$$

where $z_{\rm ref}$ is the average redshift of the z bin. Finally, we do a 3σ clip of the pixel values in the counts cutouts along the stacking axis to remove outlier pixel values. We follow the stacking procedure described in Willis et al. (2018) and create our final count rate stack, S, by using the equation

$$S = \frac{\sum_i^n C_i - \sum_i^n B_i}{\sum_i^n E_i} \tag{3.2}$$

where C is a counts cutout, B a background cutout, E a exposure map and n the number of clusters in the stack. S_1 is the count rate stack for z bin 1, with a total exposure time of 5.439×10^6 seconds. S_2 is the count rate stack for z bin 2, with a total exposure time of 1.379×10^7 seconds. S_3 is the count rate stack for z bin 3, with a total exposure time of 1.264×10^7 seconds. In addition to making cutouts centered on the SpARCS positions, error maps were made by performing the same analysis on random positions throughout the map. By using the same number of random positions from each field as clusters in the stacks, we can identify the intrinsic structures that emerge as a result of stacking within the maps, further demonstrating the presence of a significant signal in the cluster stacks. S_1, S_2, and S_3 along with their associated error maps are demonstrated in figure 3.6.

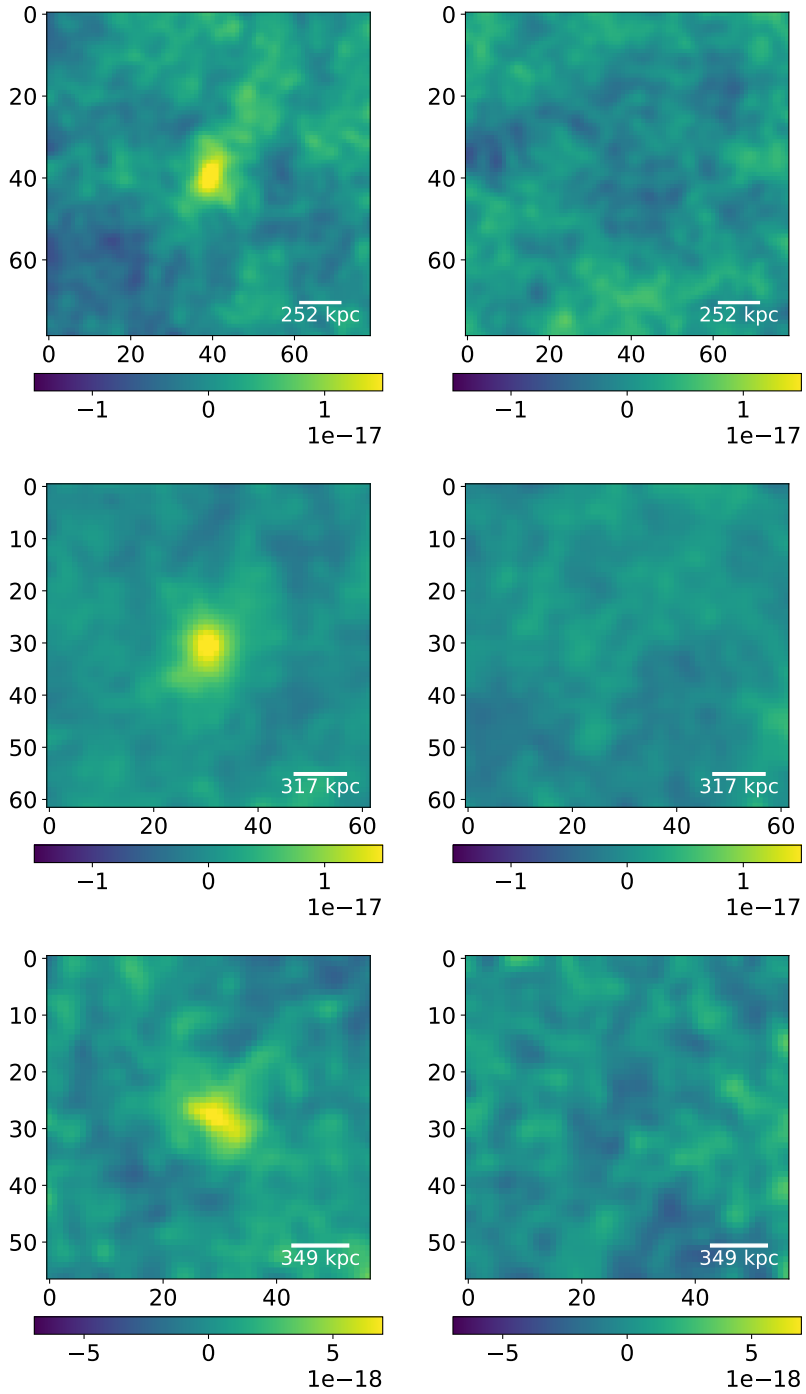

Figure 3.6: All images have been smoothed with a Gaussian kernel with $\sigma = 1.5$, pixel scale is 4"/pixel and physical scale is calculated using the mean redshift of each stack. *Top Pair:* S_1 count rate stack and error map. *Mid Pair:* S_2 count rate stack and error map. *Bottom Pair:* S_3 count rate stack and error map.

3.2.2.1 DXsC sub-sample

In addition to the stacks, the same procedure described above was done for the SpARCS clusters in the DXsC sample. However, any X-ray point sources matched with a SpARCS cluster are not masked out, and stacking is not required to measure the L_X of these clusters. Instead, we create a count rate map for each cluster individually. 140" cutouts are made, centered on the SpARCS cluster position unless the SpARCS cluster has a match with an X-ray confirmed cluster, in which case the position of the X-ray cluster is used. Each cluster's final count rate map is made by subtracting the background map from the count map and then dividing by the exposure map, similarly to equation 3.2, for the 2D cutouts.

3.3 Analysis

3.3.1 Principal Component Analysis

Although S_1, S_2, and S_3, to the best of our knowledge, do not contain X-ray point sources or confirmed clusters, we want to ensure that the X-ray emission seen in the stacks is coming from the stacked ICM rather than other sources of X-ray such as AGNs or additional X-ray point sources. The contamination of AGN in the initial SpARCS sample is expected to be insignificant (Webb et al. (2015)), but we still want to properly examine our stacks for the presence of clusters that may be dominating the stacked signal. We thus perform principal component analysis (PCA) on S_1, S_2, and S_3 to identify the dominant patterns of variation over the spatial dimension and along the stacked axis. PCA allows us to identify

any variation in the final stacked count rate map and localize which cluster(s) contribute to the variation.

We conduct PCA for a singular field by computing the empirical orthogonal functions (EOF) and the associated principal components (PC) of the data set. There are multiple ways to compute the EOFs, including Singular Value Decomposition and computation of the covariance matrix (Bjornsson and Venegas (1997)). In our analysis, we do the latter. First, the normalized matrix $\mathbf{A}$ is formed

$$\mathbf{A} = \begin{bmatrix} C_{p_n,t_1} & C_{p_n,t_2} & \cdots & C_{p_n,t_m} \\ \vdots & \vdots & \ddots & \vdots \\ C_{p_2,t_1} & C_{p_2,t_2} & \cdots & C_{p_2,t_m} \\ C_{p_1,t_1} & C_{p_1,t_2} & \cdots & C_{p_1,t_m} \end{bmatrix} \tag{3.3}$$

where $(p_1 \cdots p_n)$ represents all pixels in a map of a singular cluster in the stack, $(t_1 \cdots t_m)$ represents the different clusters in the stack, and each corresponding C value represents the counts value at that pixel. We use the Peixoto and Oort (1992) definition of covariance to calculate cov$(\mathbf{A})$

$$\text{cov}(\mathbf{A}) = \frac{1}{m}\mathbf{A}^T\mathbf{A} \tag{3.4}$$

which includes an additional factor related to the number of clusters in a stack, $\frac{1}{m}$ (Bjornsson and Venegas (1997)). The real component of the eigenvalues and eigenvectors of cov$(\mathbf{A})$ are computed. The sorted eigenvalues and vectors represent the percentage of variability and the map of spatial variability respectively. The PCs are calculated by us-

ing the equation (Bjornsson and Venegas (1997))

$$\vec{pc}_1 = \mathbf{A}\vec{x}_1 \tag{3.5}$$

where $\vec{pc}_1$ is the first principal component for the associated eigenvector $\vec{x}_1$. By examining the final EOF maps that encompass at least 50% of the variance we can identify if there are contaminating X-ray sources anywhere in our stacks. See figures 3.7, 3.8, 3.9 for initial PCA results.

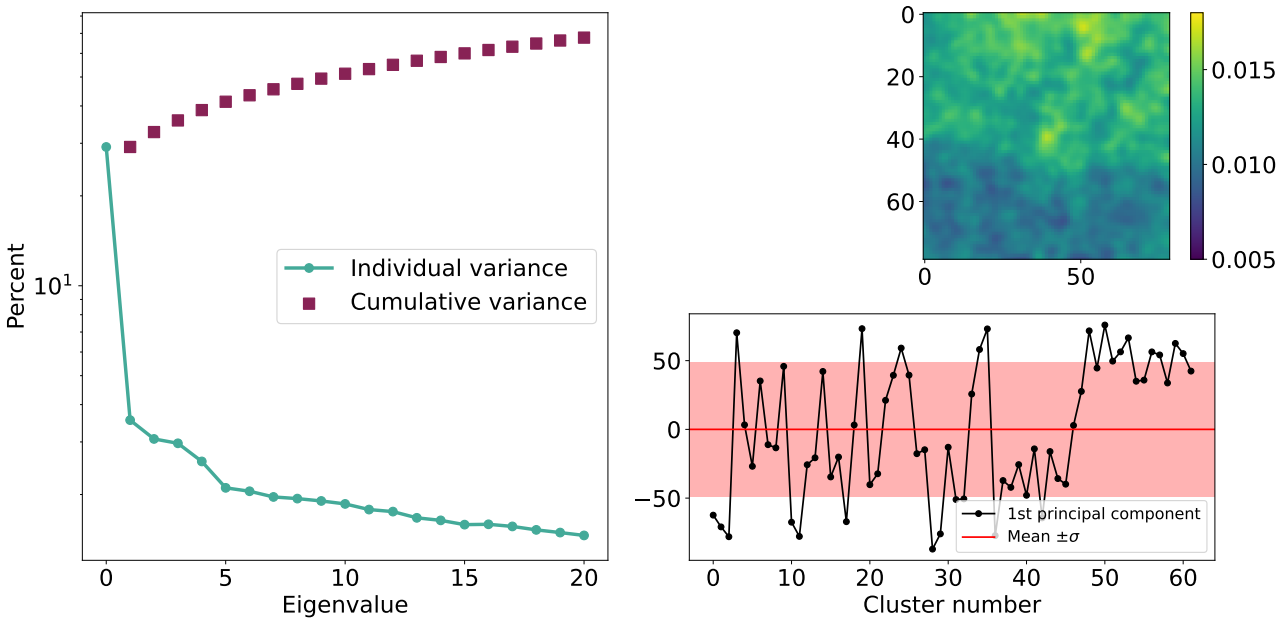

Figure 3.7: Principal component analysis results for stack S_1. *Left panel*: First 20 eigenvalues and their associated contribution to variance in the stack. The 1st eigenvalue dominates the variance. *Top right panel*: Empirical orthogonal function associated with the 1st eigenvalue for the stack, demonstrating the spatial variance. *Bottom right panel*: First principal component of each cluster.

.

For all three redshift bins, the first eigenvalue dominates the variance at $\sim 25\%$, so we focus on the spatial variance captured in the first EOF. A stack with little to no spatial

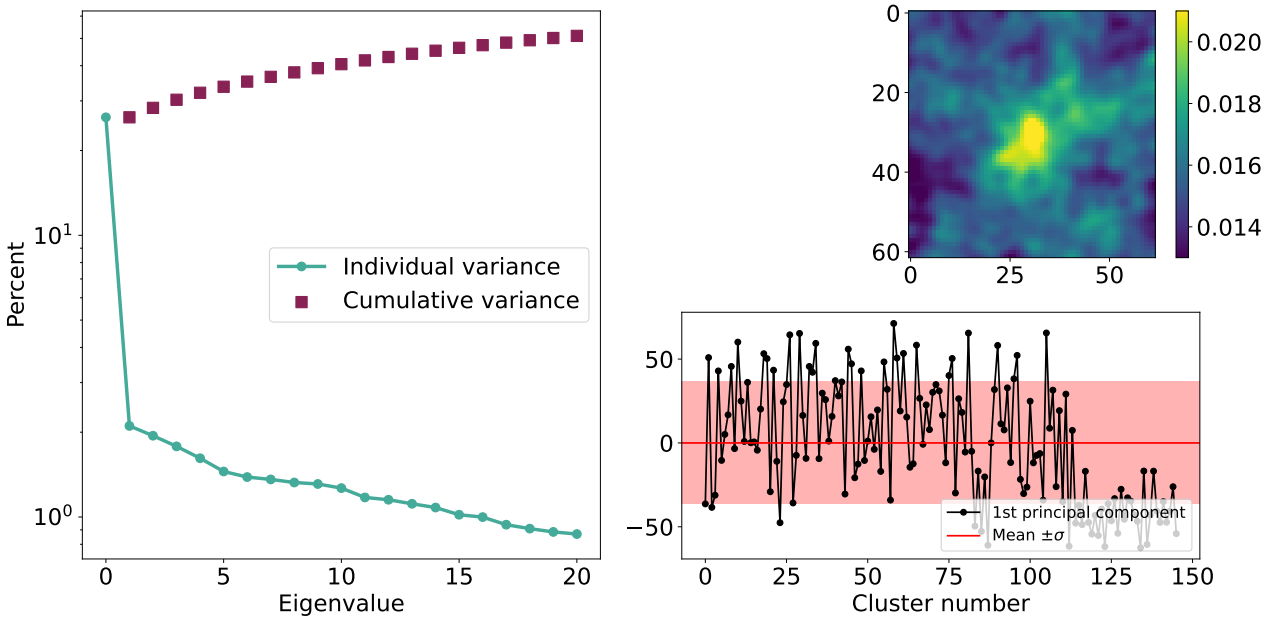

Figure 3.8: Same results as figure 3.7 for stack S_2.

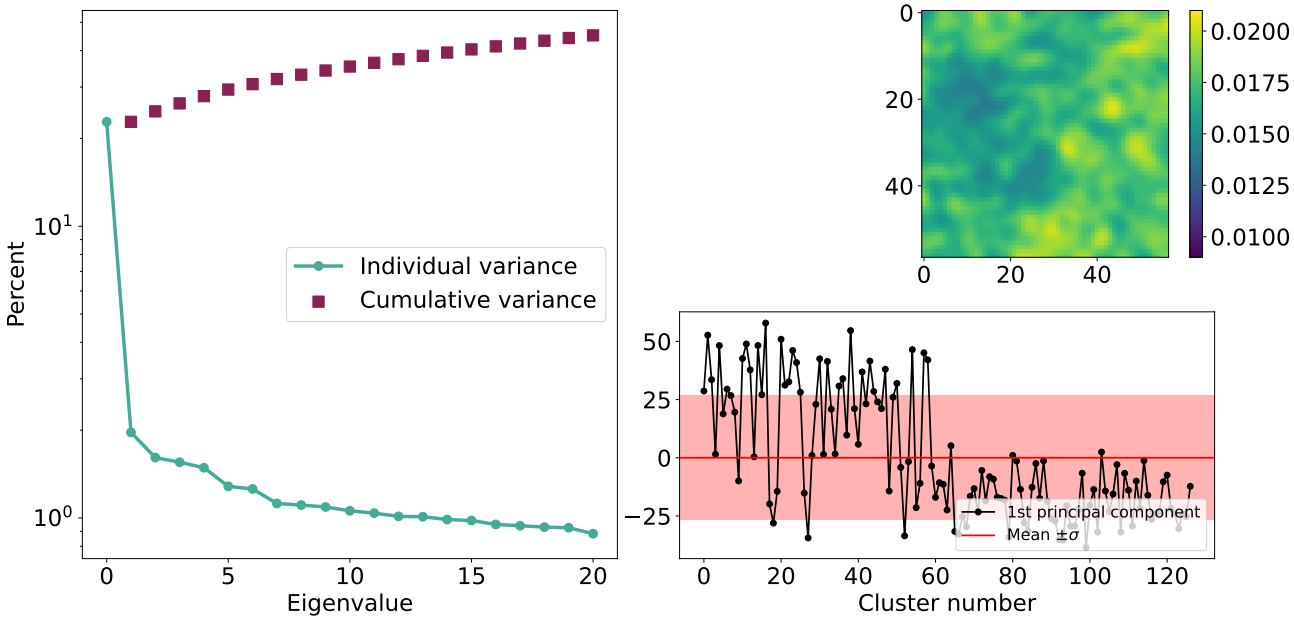

Figure 3.9: Same results as figure 3.7 for stack S_3.

variation, indicating an underlying homogeneous population, would have an EOF map with a constant value and no hot spots. As seen in figures 3.7, 3.8 and 3.9, there is slight to significant spatial variation occurring in each stack. For example, in the S_1 stack (figure

3.7) we see overall homogeneity with variation spikes in the EOF to a normalized value of ~ 0.017, but in the S_2 stack (figure 3.8) we see centralized EOF values up to > 0.021. This demonstrates that some or many clusters in each stack are contributing more to the the final stacked signal than others. The principal components (bottom right pannels in figures 3.7, 3.8 and 3.9) indicate that there is not a clear dominating culprit in the stacks, therefore requiring a second look at the clusters going into the stacks.

Individual cluster counts images with the largest 1st principal components were examined, resulting in additional X-ray point sources and X-ray-confirmed clusters being identified. These sources were added to the mask, and the associated SpARCS clusters moved from the UXsC sub-sample to the DXsC sub-sample.

In addition to contaminating sources, some SpARCS clusters in the UXsC sample were found to be X-ray bright and dominating the variance. We, therefore, define an additional condition for SpARCS clusters if they are to be included in the UXsC sample and hence the X-ray undetected stack. We use the low count statistics of Kraft et al. (1991) for a general definition of X-ray detection. For events that follow a Poisson distribution, a Bayesian confidence interval can be calculated for a given confidence level, number of observed counts, and number of background counts (Kraft et al. (1991)). We use the confidence intervals for the 0.90 confidence level, which are tabulated for a range of counts and backgrounds (see Kraft et al. (1991)). We linearly interpolate the Kraft table and extract the mean number of counts and background counts for a 150 kpc radius aperture centered on each SpARCS cluster position. We define a detectable source as having a lower confidence interval of > 0.1 and move any SpARCS clusters that meet this criterion from the UXsC to the DXsC sub-sample. Many, but not all, of the clusters, identified as X-ray detectable by

the lower confidence level were already in the DXsC sub-sample as the cluster positions were matched with an X-ray source or a confirmed cluster prior to the PCA.

We re-do the stacking procedure described in section 3.2.2 with the updated UXsC sample of non-detected X-ray clusters after removing new SpARCS associated X-ray sources found with PCA and SpARCS clusters that meet the Kraft criterion. These stacks will be referred to as $S_{1,final}$, $S_{2,final}$ and $S_{3,final}$ and are shown in figure 3.13. Updated PCA done on the $S_{1,final}$, $S_{2,final}$ and $S_{3,final}$ stacks are demonstrated in figures 3.10, 3.11 and 3.12. Compared to the PCA done on S_1, S_2, and S_3, the new stacks show equal or less spatial variance. Finding additional associated sources and adding the Kraft criterion gives more confidence, particularly in the $S_{2,final}$ stack, that the signal is not dominated by only a few X-ray-detected clusters. With reduced EOF map values, we conclude that to first order, the population of clusters in each stack is relatively homogeneous. Unless otherwise specified, the updated UXsC sub-sample resulting in the $S_{1,final}$, $S_{2,final}$, and $S_{3,final}$ stacks is used in the remainder of the analysis.

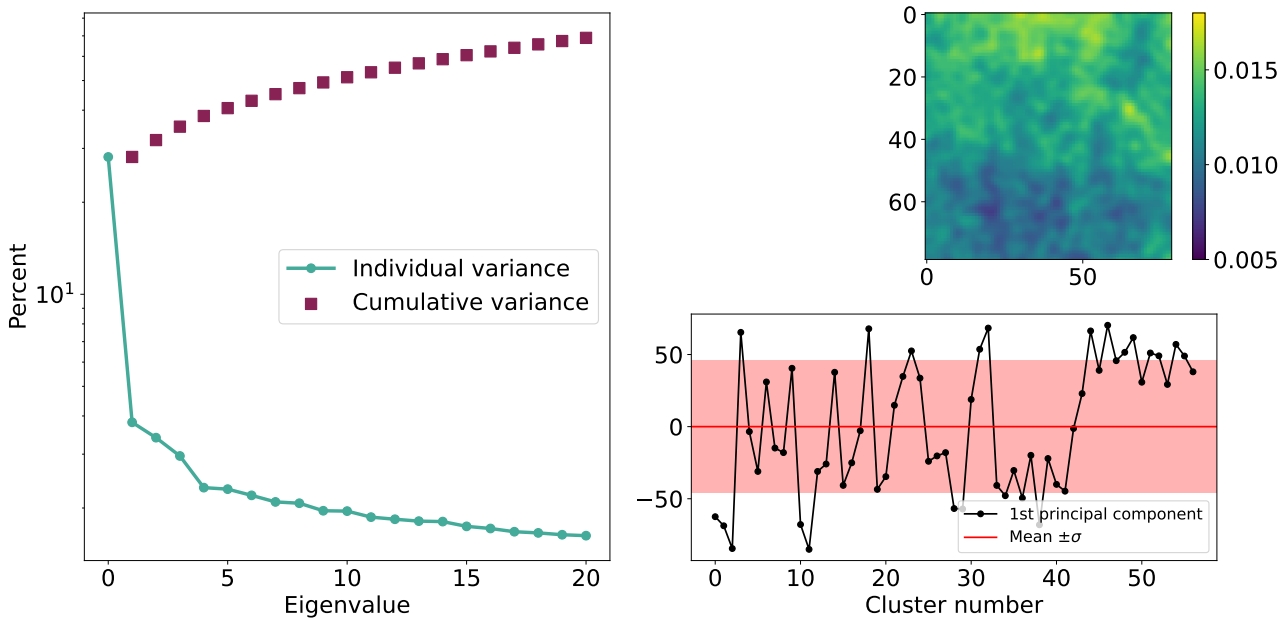

Figure 3.10: Principal component analysis results for stack $S_{1,final}$. *Left panel*: First 20 eigenvalues and their associated contribution to variance in the stack. The 1st eigenvalue dominates the variance. *Top right panel*: Empirical orthogonal function associated with the 1st eigenvalue for the stack, demonstrating the spatial variance. *Bottom right panel*: First principal component of each cluster.

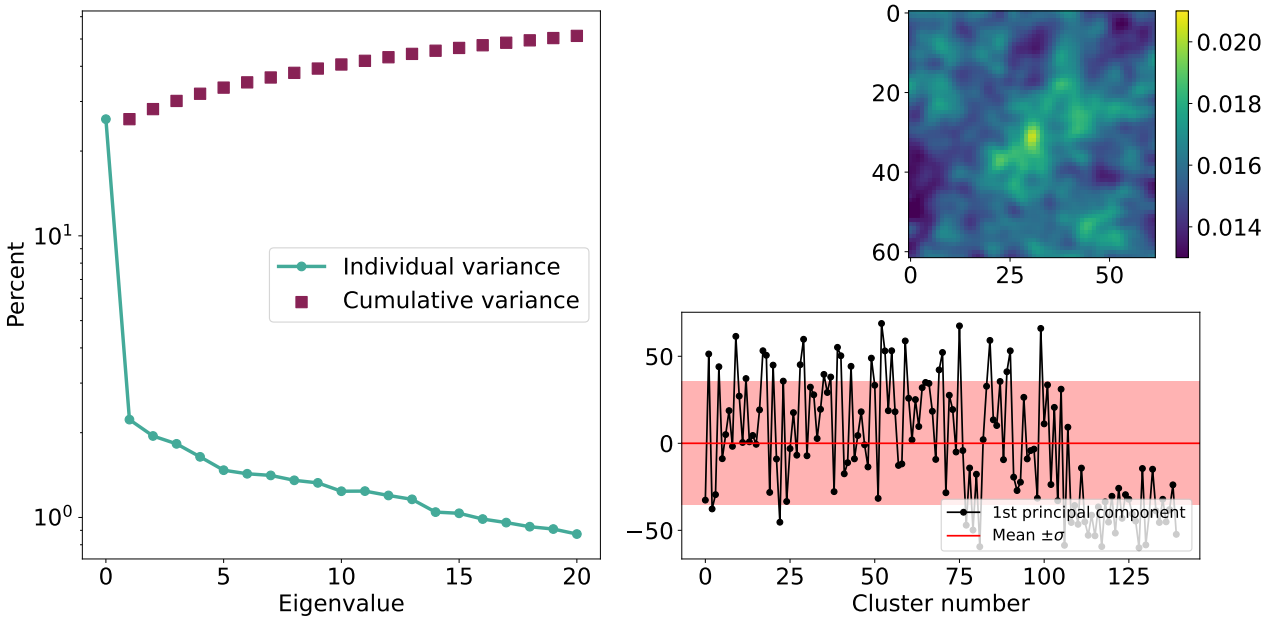

Figure 3.11: Same results as figure 3.10 for stack $S_{2,final}$

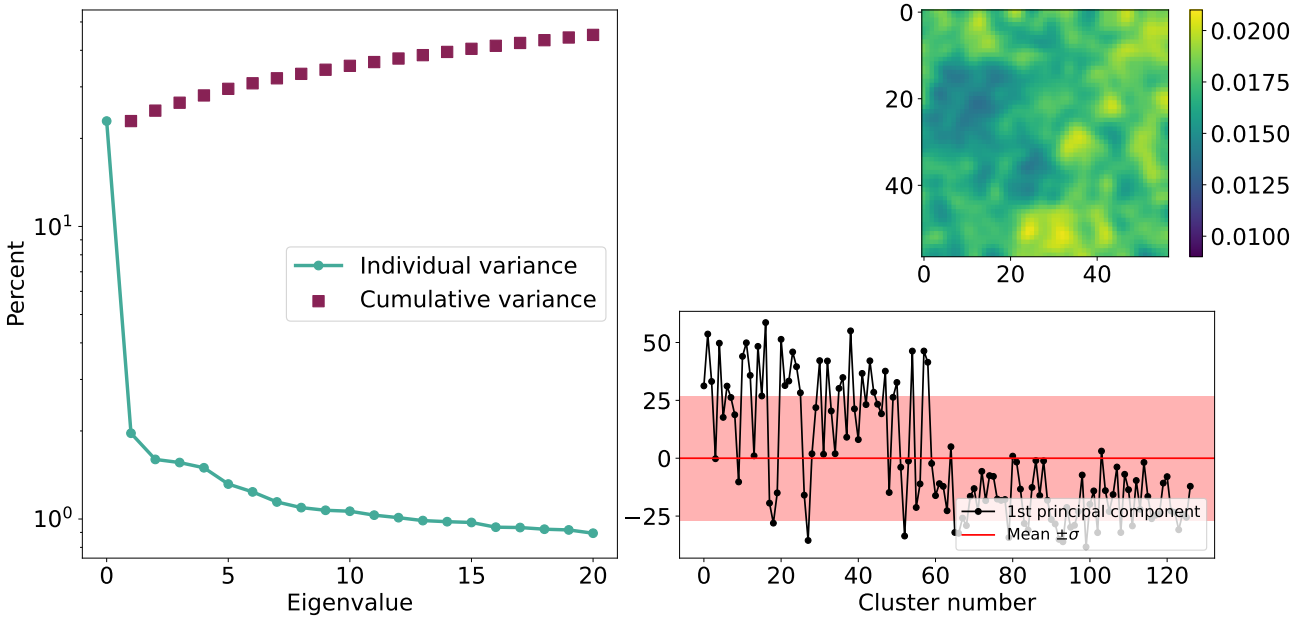

Figure 3.12: Same results as figure 3.10 for stack $S_{3,final}$

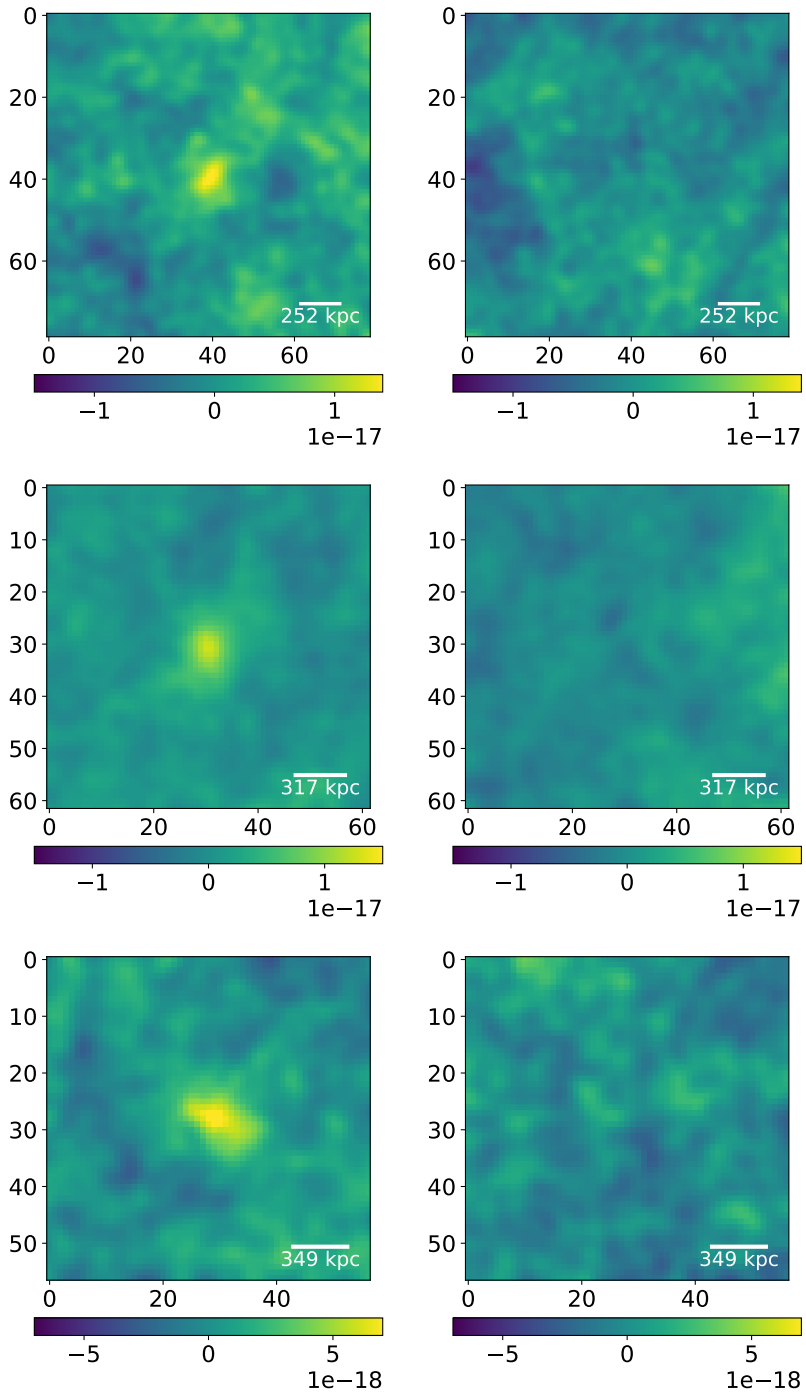

Figure 3.13: All images have been smoothed with a guassian kernal with $\sigma = 1.5$, pixel scale is 4"/pixel and physical scale is calculated using the mean redshift of each stack. Clusters detected with Kraft criterion are excluded from stack. *Top Pair:* $S_{1,final}$ count rate stack and error map. *Mid Pair:* $S_{2,final}$ count rate stack and error map. *Bottom Pair:* $S_{3,final}$ count rate stack and error map.

3.3.2 Radial Brightness plots

With a robust signal from stacking not dominated by a single cluster or contaminating point source, an average X-ray luminosity can be extracted for clusters not individually detected in the X-ray. To calculate these luminosities we use the $S_{1,final}$, $S_{2,final}$ and $S_{3,final}$ stacks. To convert from a count rate to a flux, we used an energy conversion factor (ECF). Each field and *XMM-Newton* detector (PN, MOS1, MOS2) has a different ECF and is summarized in table 3.3.

Table 3.3: Summary of energy conversion factors for the soft X-ray band (0.5-2 keV) fluxes for each detector and field as identified in Chen et al. (2018) and Ni et al. (2021). All factors have units of 10^{-11} erg cm^{-2} s^{-1}/counts s^{-1}.

Field	PN	MOS1	MOS2
XMM-LSS	$\frac{1}{6.23}$	$\frac{1}{1.78}$	$\frac{1}{1.76}$
W-CDF-S	$\frac{1}{8.57}$	$\frac{1}{2.27}$	$\frac{1}{2.28}$
ELAIS-S1	$\frac{1}{8.03}$	$\frac{1}{2.21}$	$\frac{1}{2.21}$

Three ECFs (ECF_{XMM}, ECF_{CDFS}, ECF_{ES}) are calculated for each field from an average of the three detectors. For each stack, the final ECF is calculated by averaging the three field ECFs for a final value of 3.684×10^{-12} erg s^{-1} cm^{-2}/counts s^{-1}, which is multiplied by the final count rate maps. Using the software package PYPROFFIT (Eckert et al. (2020)), each stack is used to create a surface brightness profile as a function of radii using circular annuli centered on the map's brightness peak. PYPROFFIT is the python version of Proffit C++. Both packages allow for the analysis of X-ray brightness profiles of galaxy clusters. In addition to the surface brightness of the signal, we include the surface brightness of the error maps (as seen in figure 3.13) and an average point-spread function (PSF) for our three fields. We follow a method discussed in Anderson et al. (2015) and use the

point source catalog in each field to create a point source stack and measure the surface brightness to obtain the PSF. The PSF is normalized to the central signal brightness.

We use the Fitter class in PYPROFFIT, which performs maximum-likelihood optimization for a given model. β- models are commonly used to capture the shape of an X-ray radial profile of a galaxy cluster, which is extended out to large radii due to the hot ICM gas emission (Arnaud (2009)). We thus fit the β-model in PYPROFFIT

$$I(r) = I_0(1 + (x/r_c)^2)^{-3\beta+0.5} + B \tag{3.6}$$

to the surface brightness of our signal maps to obtain best-fit values for parameters I_0, r_c, β, B and a reduced χ^2 value of the model fit. See figures 3.14, 3.15, 3.16.

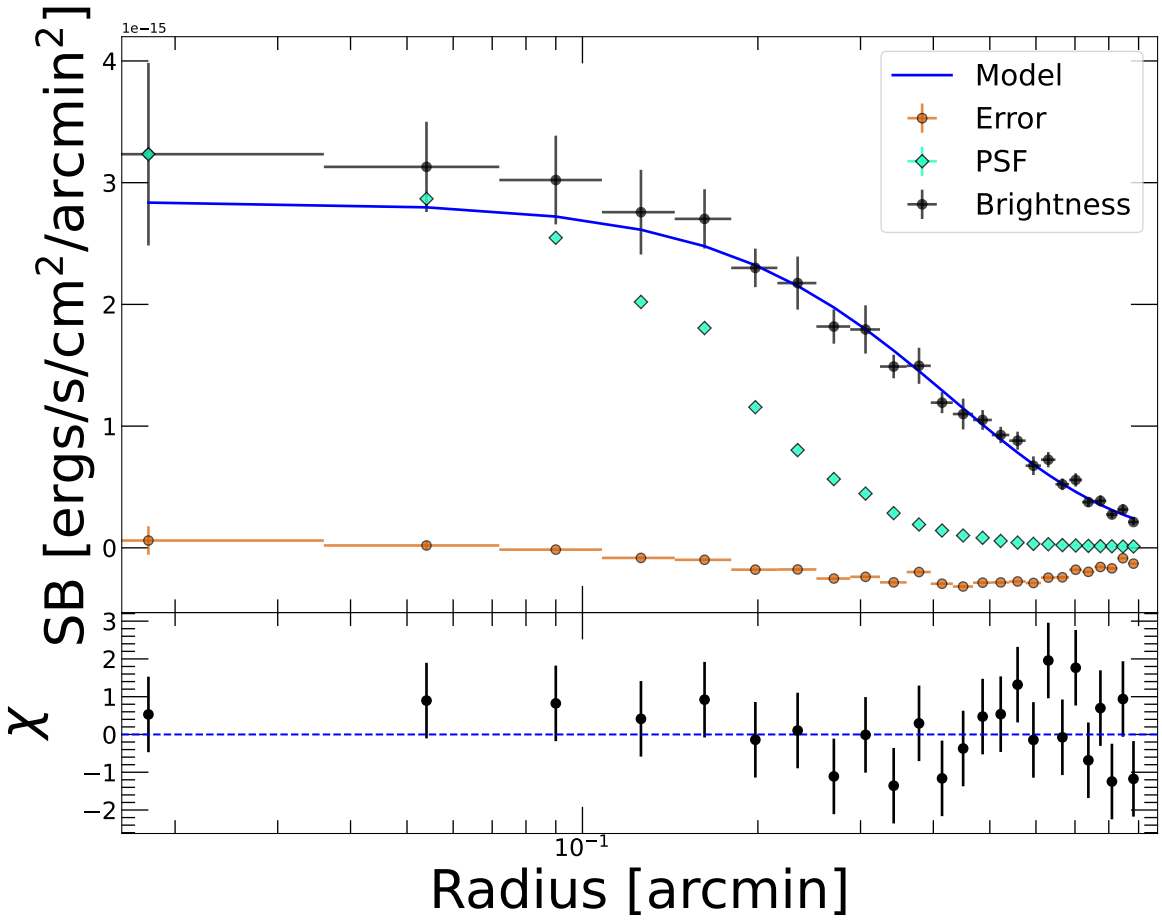

Figure 3.14: Surface brightness radial plot for the $S_{1,final}$ stack. The early fall-off of the centrally-normalized point spread function (PSF) relative to the signal demonstrates the extended nature of the X-ray emission from the stacked clusters out to order hundreds of kpc. β-model fit residuals are shown in the bottom panel.

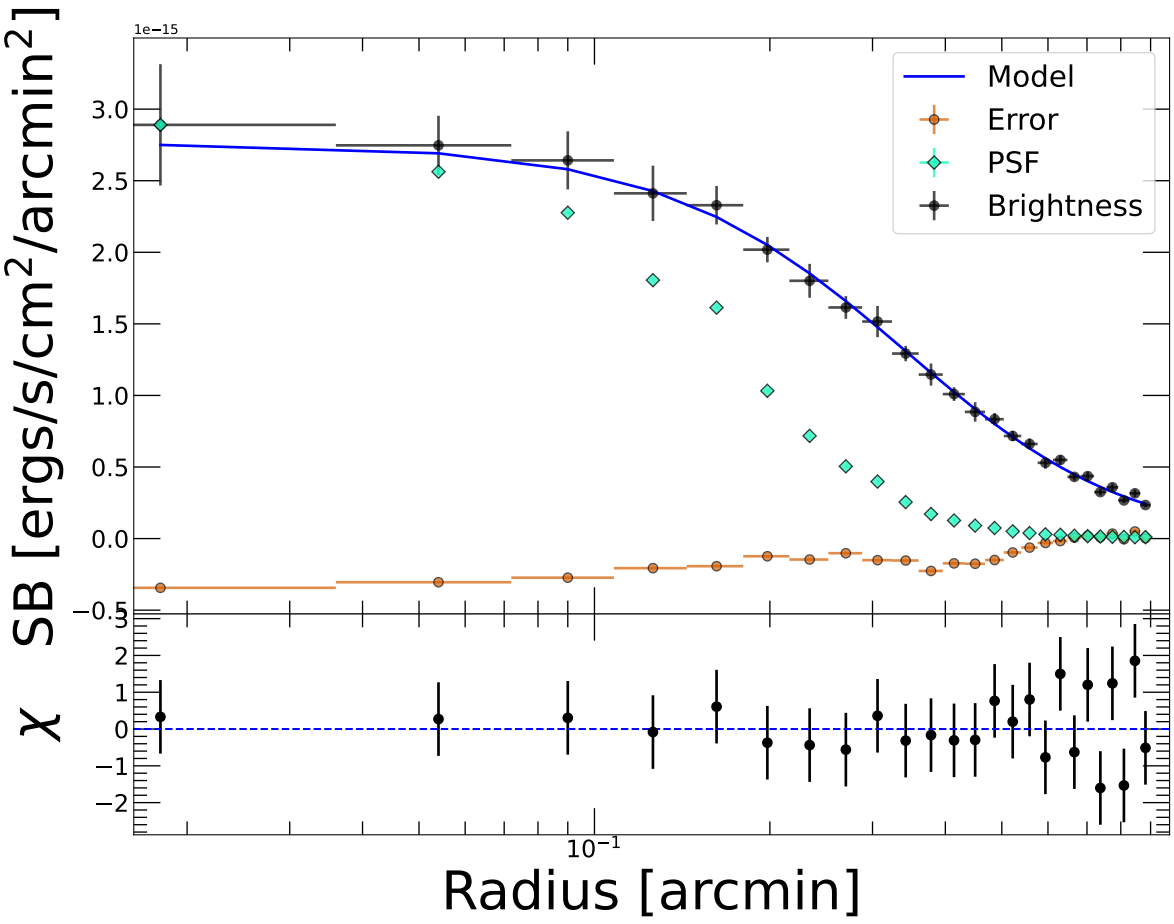

Figure 3.15: Surface brightness radial plot for the $S_{2,final}$ stack. The early fall-off of the centrally-normalized point spread function (PSF) relative to the signal demonstrates the extended nature of the X-ray emission from the stacked clusters out to order hundreds of kpc. β-model fit residuals are shown in the bottom panel.

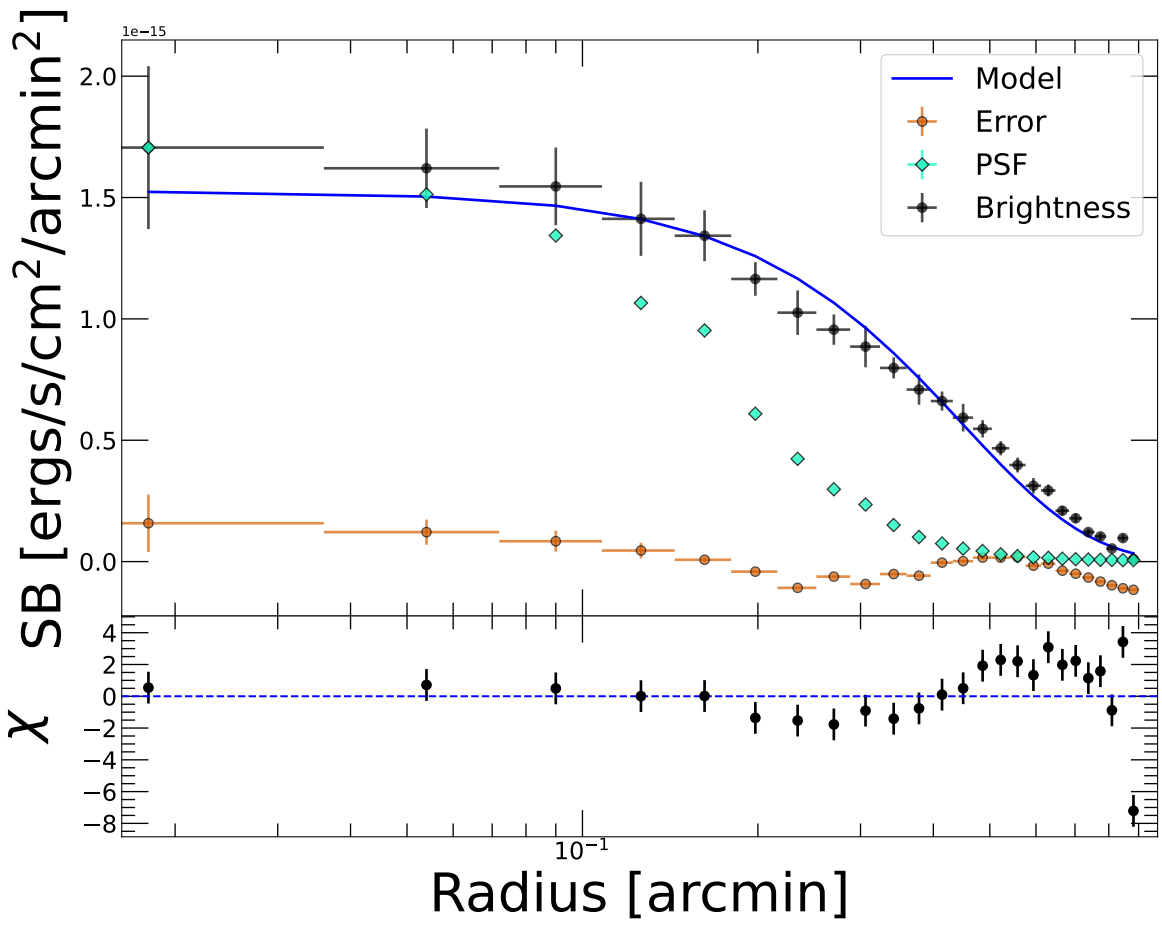

Figure 3.16: Surface brightness radial plot for the $S_{3,final}$ stack. The early fall-off of the centrally-normalized point spread function (PSF) relative to the signal demonstrates the extended nature of the X-ray emission from the stacked clusters out to order hundreds of kpc. β-model fit residuals are shown in the bottom panel.

For each redshift bin stack, the model is integrated along the solid angle of the cluster out to a radius of 300 kpcs converted to arcminutes using the average redshift of each stack. The final integrated flux, F, is then converted to an X-ray luminosity, L_X, using the equation

$$L_X = (4\pi D_L)F \tag{3.7}$$

where D_L is the angular diameter distance obtained from the average redshift of the stack. Errors on the luminosity are calculated by fitting another β- model to the upper error bars on the signal profile, integrating along the same radii, and doing the same flux to luminosity conversion. Section 3.3.3 contains an additional discussion of errors in the stacks. Luminosity measurements for each redshift bin are summarized in table 3.4.

Table 3.4: Final luminosities measured from the integrated β-model fit to the radial brightnesses of the stack for each z bin inlucding reduced χ^2 values for each fit. Error listed for luminosities are errors induced measuring the surface brightness and do not reflect the global error of the underlying population.

Stack	L_X (0.5-2 keV) [$\times 10^{42}$ erg s^{-1}]	χ^2/ν	Avg Ngal
$S_{1,final}$	2.005 ± 0.206	$21.455/21$	7.427 ± 4.794
$S_{2,final}$	5.868 ± 0.449	$17.831/21$	9.272 ± 5.578
$S_{3,final}$	12.477 ± 1.043	$114.308/21$	11.428 ± 6.847

The same process described above is repeated for the individual count-rate maps made for the DXsC sub-sample clusters. The X-ray luminosity is measured to the same radii of 300 kpcs, with the physical to image conversion done using the redshift of the individual cluster. Errors on the individual luminosities are measured in the same way as described above. DXsC luminosities dominated by their errors are discarded and not included in the remainder of the analysis.

3.3.3 Bootstrapping

Although the $S_{1,final}$, $S_{2,final}$ and $S_{3,final}$ stacks provide average L_X and Ngal measurements for clusters not detected in the X-ray, we want to fully understand the spread of richness and X-ray luminosities of the underlying population in these stacks. We rely

on bootstrapping to examine the errors in the X-ray luminosity calculation induced by slight differences in our stacking population. In each redshift bin, 1,000 bootstrap stacks are created, with replacement, from the final population of clusters used to create the $S_{1,final}$, $S_{2,final}$ and $S_{3,final}$ respectively. The average richness and redshift of the clusters randomly picked for each stack are measured. The analysis described in section 3.3.2 is repeated to create a surface brightness profile and measure the luminosity from each bootstrap stack. The result is 1,000 X-ray luminosities and associated average richnesses for each redshift bin. Bootstrapping analysis examines what the luminosity of a stack could be given that the central X-ray brightness of each cluster may be varied due to a range of physical differences in the cluster population.

In figure 3.17, we compare the spread of L_X and richnesses calculated with the bootstrapping analysis to the results listed in table 3.4 using kernel density estimation (KDE) plots (Waskom (2021)). We note that our average values of L_X and Ngal, as listed in table 3.4 align well with the peaks of the probability distributions for both variables. However, the bootstrapping allows for a transparent display of the global error present in each stack's L_X calculation, which is not captured by the measurement errors reported in table 3.4.

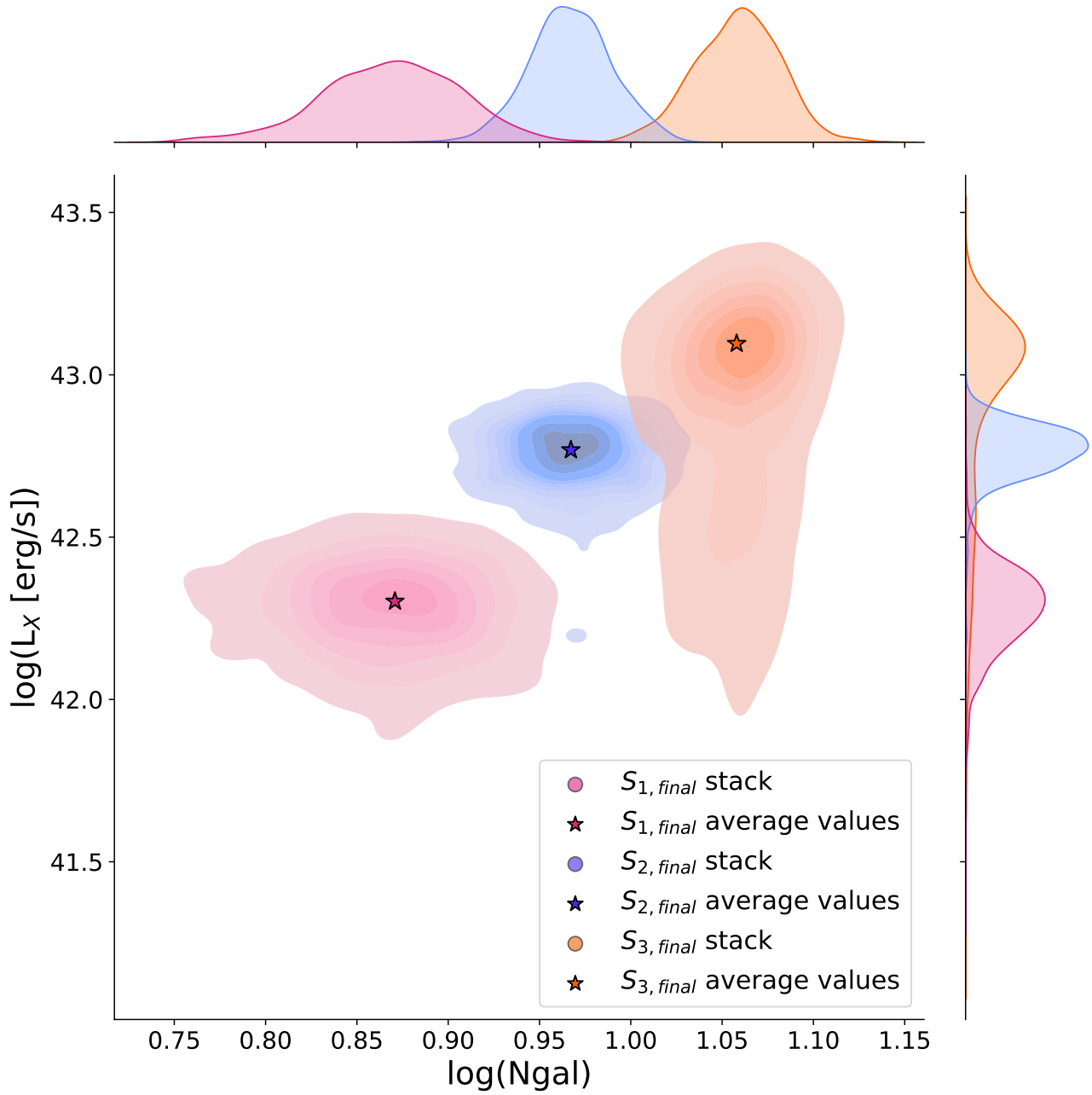

Figure 3.17: Bootstrap results for final stacks. Darker contours represent higher probabilities that the randomly stacked underlying population will generate the associated L_X and Ngal values. Stars represent the average values for each stack as listed in table 3.4.

3.4 Results

3.4.1 L_X-Ngal Relation

Given our DXsC sub-sample with directly measured L_X and the bootstrap results from our UXsC sub-sample stacks, we can directly compare where each sub-samples lie in the L_X vs. Ngal space. This allows us to directly examine how the populations of optically and X-ray-detected clusters compare with those only detected in the optical. We show the DXsC sub-sample for each redshift bin as individual points and the bootstrap results as a KDE.

For the individual points of the DXsC sub-sample, we conduct a Bayesian linear regression using a Python adaption of Kelly (2007)'s LINMIX IDL package. This fitting routine is often used for the L_X-Ngal relation as the routine handles measurement errors on both X and Y and intrinsic scatter present in the relation (Rykoff et al. (2008)). During the regression, Bayesian inference is employed, and a Markov chain containing random draws from the posterior is developed (Kelly (2007)). Convergence of the MCMC is eventually achieved, which is defined as a R-hat (potential scale reduction factor) of < 1.1 (see Gelman and Buja (2004), Kelly (2007)).

To account for the probability that approximately 15% of the DXsC sub-sample points were spurious matches, as discussed in section 3.2.1 and figure 3.4, we conduct 50 repetitions of the LINMIX fitting, each time randomly removing 15% of the DXsC points that were classified as an X-ray point source match. The final coefficients (α, γ, ϵ) obtained for the linear fit $y = \alpha + \gamma x + \epsilon$ are calculated from the average of the 50 α, γ and ϵ generated. Final errors on each parameter are propagated from the 50 errors generated. This corrects

for the presence of the spurious points as the final fits and errors contain the additional scatter. Final coefficients and associated errors for each z bin are listed in table 3.5.

Table 3.5: For each z bin, mean of 50 best-fit slope (γ), y-intercept (α) and intrinsic scatter (ϵ) coefficients from LINMIX linear regression fitting and associated propagated errors. Fits describe scatter and measurement errors in the DXsC cluster sample.

z bin	α	γ	ϵ
1 $(0.4 \leq z \leq 0.6)$	42.374 ± 0.358	1.282 ± 0.309	0.505 ± 0.082
2 $(0.6 < z \leq 1.1)$	43.286 ± 0.421	0.257 ± 0.373	0.456 ± 0.061
3 $(1.1 < z \leq 1.9)$	42.589 ± 0.325	0.671 ± 0.297	0.388 ± 0.072

Final results for the L_X-Ngal relation, including results from the LINMIX fitting to the DXsC points, are shown in figure 3.18, 3.19 and 3.20 for z bins 1, 2 and 3 respectively.

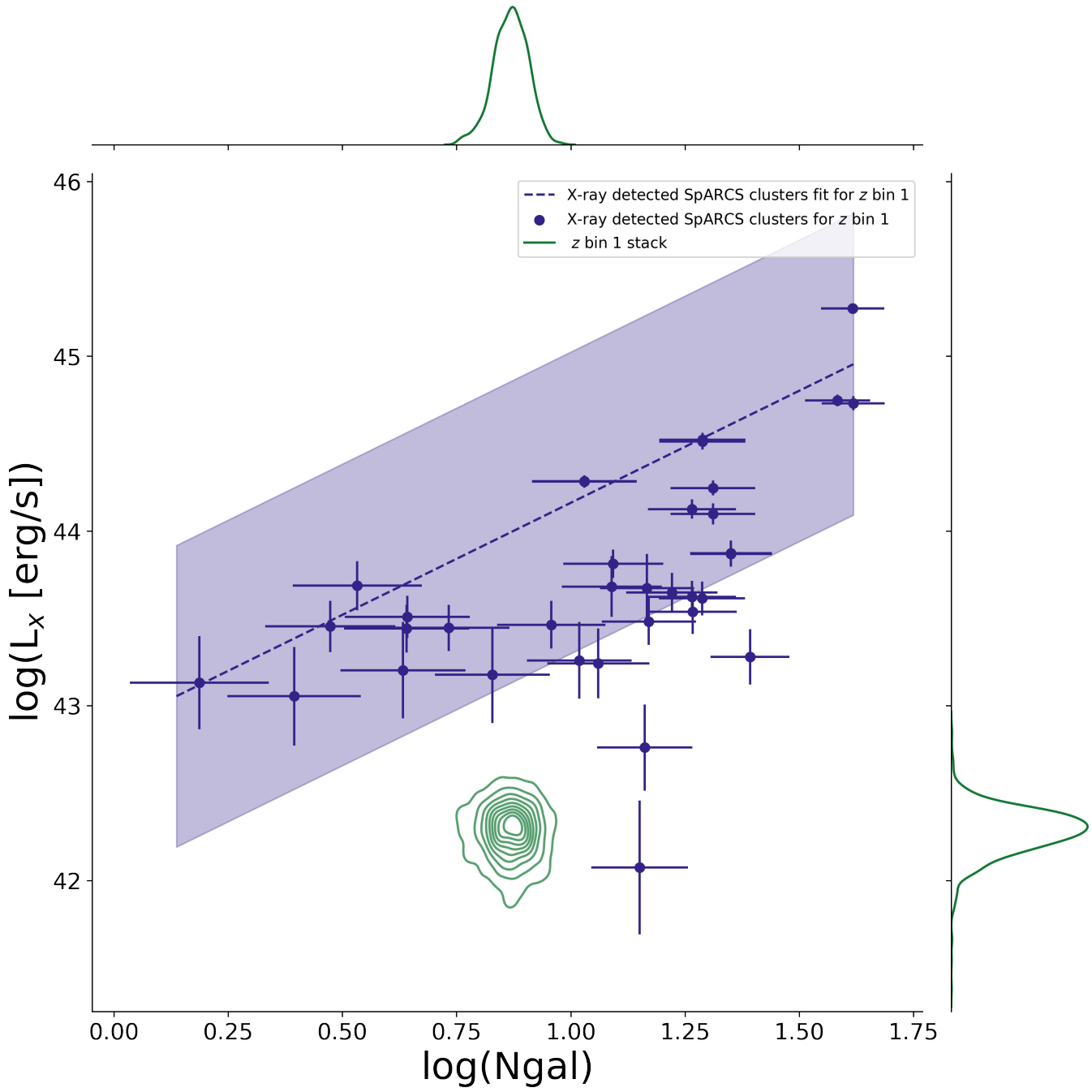

Figure 3.18: Final L_X-Ngal relation for the z 1 bin DXsC sub-sample (purple scatter points) with the bootstrap results for the z 1 bin UXsC stack overlaid (green contours). The best-fit linear regression to the DXsC is included.

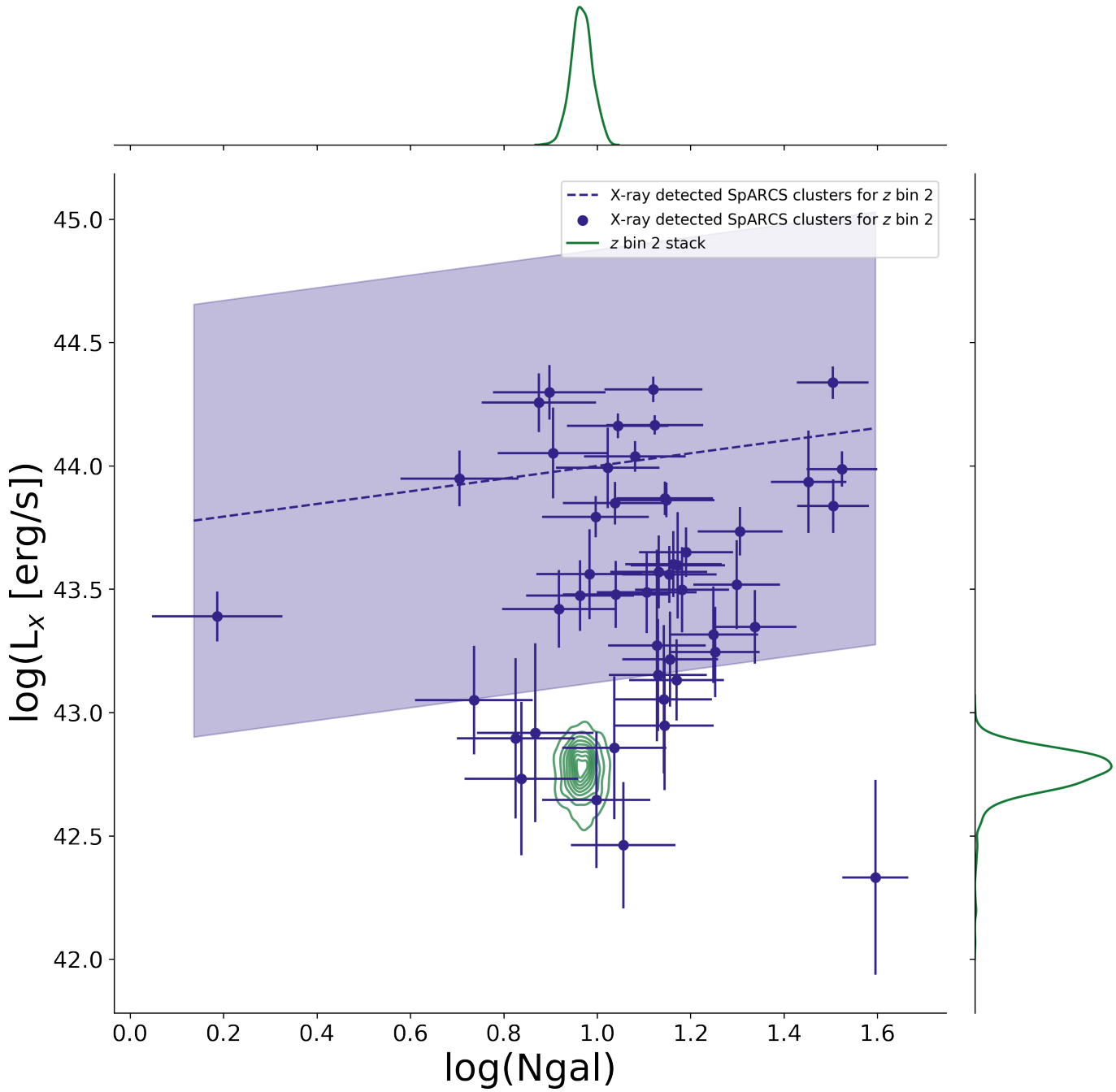

Figure 3.19: Final L_X-Ngal relation for the z 2 bin DXsC sub-sample (purple scatter points) with the bootstrap results for the z 2 bin UXsC stack overlaid (green contours). The best-fit linear regression to the DXsC is included.

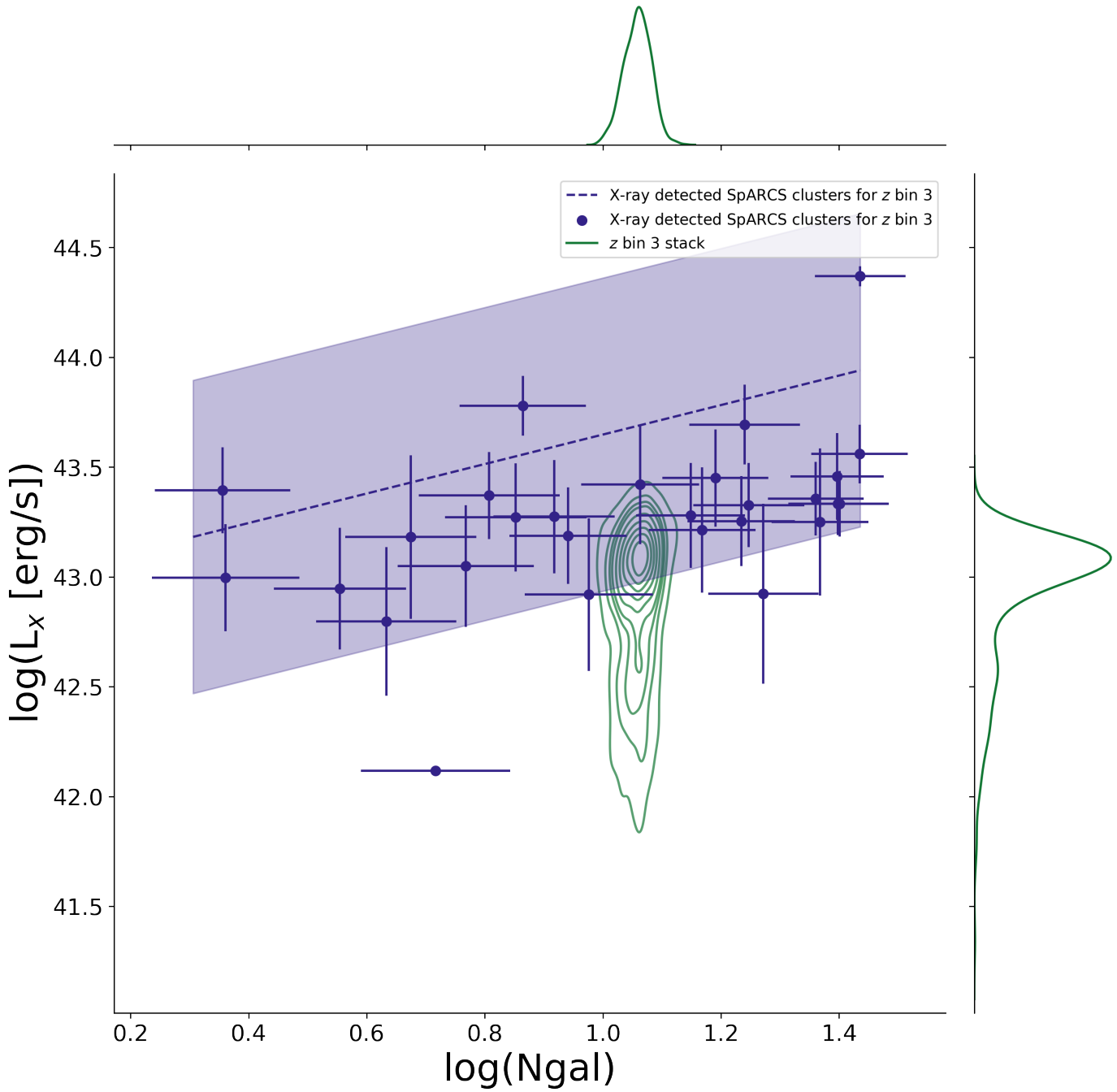

Figure 3.20: Final L_X-Ngal relation for the z 3 bin DXsC sub-sample (purple scatter points) with the bootstrap results for the z 3 bin UXsC stack overlaid (green contours). The best-fit linear regression to the DXsC is included.

In addition, we examine the redshift evolution of the linear regression models for the DXsC points. This redshift evolution is demonstrated in figure 3.21. We examine the redshify evolution for just the DXsC sources as the results from the UXsC stacks contribute only a single point for each redshift bin to the relation and are, therefore, challenging to examine independently.

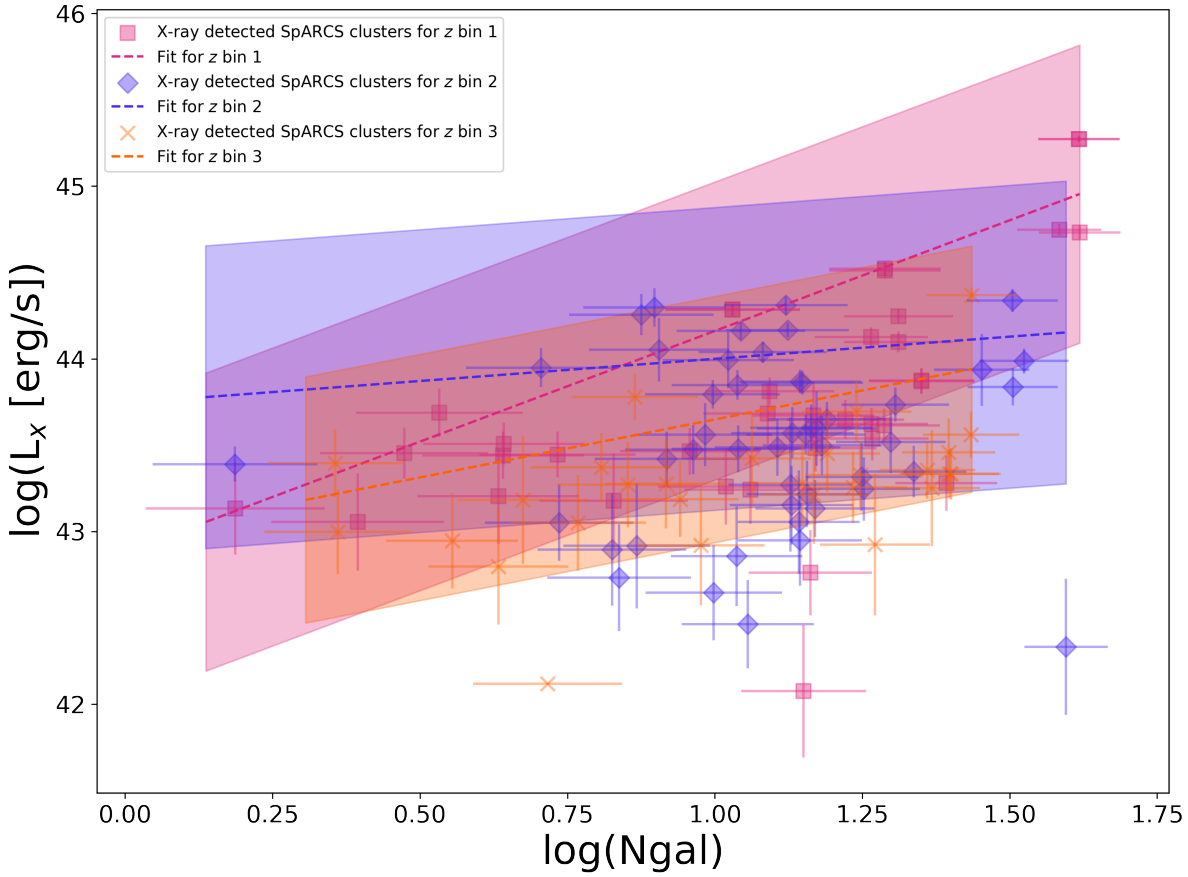

Figure 3.21: DXsC for each z bin with associated linear regression fit shown. z bin 1 clusters ($0.4 \leq z \leq 0.6$) are represented by pink squares, z bin 2 clusters ($0.6 < z \leq 1.1$) are represented by purple diamonds, and z bin 3 clusters ($1.1 < z \leq 1.9$) are represented by orange crosses.

Chapter 4

Discussion of Findings

4.1 Stacks and Radial Plots

Overall, we are able to find a significant X-ray signal by stacking on X-ray un-detected clusters, with positions identified using optical and IR data. These stacks (as seen in figure 3.13) show extended spherical emission from the SpARCS positions with count rates significantly higher than randomly stacked positions in the fields. These stacks do not contain X-ray detected clusters, potential misclassified point sources, or clusters with X-ray emission dominated by AGN, as demonstrated by our principal component analysis. Therefore, the stacked signal represents the X-ray emission from the ICM of the underlying clusters when observed in the X-ray at extended exposures. Our redshift bins ensure that the significant variations in angular diameter distances between local and distant clusters are accounted for and allow us to stack in image space.

With a large PSF, the high central flux of an X-ray observation can be smeared to high radii. When this occurs, the fictitious flux, parading as extended emission, can be mis-

taken for the ICM (Mohr et al. (1999)). The sustained high flux values in our radial surface plots beyond the radii which signifies the PSF falloff of our fields ($\sim$ 0.2 arcmin), indicates the presence of physical emission and the confirmation that we are examining cluster populations. In z bin 1 ($0.4 \leq z \leq 0.6$), we measure significant extended emission out to a radius of 340 kpcs, in z bin 2 ($0.6 < z \leq 1.1$) to a radius of 435 kpcs and in z bin 3 ($1.1 < z \leq 1.9$) to a radius of 415 kpcs, all values well within the expected radii of a galaxy cluster. The β- model fit to the radial profile of $S_{1,final}$ and $S_{2,final}$ have decent goodness of fits of χ^2= 21.455 for 21 d.o.f and χ^2= 17.831 for 21 d.o.f respectively. The goodness of fit for the $S_{3,final}$ radial profile is not as strong at χ^2= 114.308 for 21 d.o.f, which we attribute to the slightly non-spherical nature of the final stacked emission. Morphological differences are expected of clusters in the $z > 1.1$ regime as the systems are still forming. This may lead to increased dynamical disturbance and offsets between the BCG and X-ray peak positions. However, from visual examination, the radial plot for $S_{3,final}$ (3.16) still demonstrates physical extended emission and is still used in the remainder of the analysis, with the caveat that the resulting L_X may contain a higher amount of error.

In optical selection methods, projection effects can be a significant source of error (Cohn et al. (2007), Costanzi et al. (2019), Sunayama et al. (2020)). However, our results show that the clusters in our optically selected sample are either matched with a known X-ray cluster, misclassified point source, or contribute to physical extended X-ray emission through stacking. We, therefore, regard projection effects as a minimal error in the sample of optically selected clusters used.

4.2 Observational biases in the L_X-Ngal Relation

Overall, it is very challenging to directly compare our X-ray luminosity vs. optical richness scaling relation results to those that exist in the literature (see Rykoff et al. (2008), Gal et al. (2009), Giles et al. (2022), Upsdell et al. (2023)). This is primarily due to the differences in optical richness definitions. It is also non-trivial to convert different optical richness as many depend on the flux limit of the survey, the size of the aperture, and whether the aperture size is measured in physical space or based on a z-dependent critical radius (Rykoff et al. (2008)). Therefore our comparisons are made in a relative manner.

One of our guiding research questions is, do X-ray selected clusters agree with only optically selected clusters in the L_X-Ngal relation? In our lowest redshift bin (figure 3.18), we see the bootstrap results of the UXsC clusters sitting more than a dex below the L_X of the DXsC clusters for a given redshift. However, it is challenging to conclude from these results as the redshifts represented in this bin are highly prone to selection effects in the X-ray. It is challenging to know if the scale of the X-ray luminosity of the DXsC clusters is independent of the fact that the more X-ray luminous clusters are observationally favored at these redshifts and if the UXsC clusters are, therefore, intrinsically less luminous in the X-ray or fit within the scatter of the relation. However, in similar studies such as Giles et al. (2022), a large sensitivity on selection methods was seen while identifying where a population of clusters lie on the L_X-Ngal relation at low redshift.

In the middle redshift bin (figure 3.19), we see a clearer picture of where the UXsC clusters sit in relation to the DXsC population. The broader spread in the L_X values of the DXsC clusters indicates that the UXsC clusters are within the scatter of the relation. This

same result is seen in our highest redshift bin (figure 3.20). However, it is less significant as the UXsC cluster population has a much higher error on its X-ray luminosity.

For the higher redshift bins, we are seeing a result that is consistent with the literature, that X-ray selection methods pick out clusters with a higher L_X relative to the optical clusters (Rykoff et al. (2008), Gal et al. (2009)). However, we see the populations of non-X-ray detected clusters represented by the scatter of the scaling relations established with only X-ray-selected clusters. At the lower redshifts ($z < 0.6$), we may be limited by selection effects when making this conclusion. However, the findings in this bin do indicate that there does exist a population of clusters at the same richness that will represent the lower end of the X-ray luminosity selection function. It is, therefore, imperative when creating large-scale cluster surveys with X-ray detection methods that additional selection techniques are used to probe the low richness and X-ray luminous population. This analysis, along with many others (Dai et al. (2007), Rykoff et al. (2008), Willis et al. (2018)) demonstrates the power of stacking in the X-ray to understand the X-ray properties of the clusters that may lie below flux limits. This aids with identifying the "floor" of cluster luminosity and, therefore, mass, indicating that those models are incomplete with only X-ray-selected clusters, especially at low redshift.

4.3 Redshift Evolution

Another goal of this work is to examine the evolution of the L_X-Ngal relation as a function of redshift. As we only have a single Ngal value for each redshift bin in the UXsC population, we solely use the DXsC population and results from the linear regression for

this result (figure 3.21). In a similar analysis, Rykoff et al. (2008) sees their high redshift bin (avg $z = 0.23$) cluster stacks to be almost twice as bright at clusters at the same richness but lower redshift (avg $z = 0.14$). They note that this is more extreme than would be expected of a change in L_X for different redshifts at a given mass (a common proxy for richness), which should follow $L_X \propto \rho_c(z)^{7/6}$ (Kaiser (1986), Rykoff et al. (2008)). They attribute the significant variation in L_X to the redshift variation present in their optical richness measurement (N_{200} = number of red-sequence galaxies brighter than 0.4 L_* within a scaled aperture R_{200}) at fixed mass which would reduce the amount of dependence of the L_X-Ngal relation on redshift (Rykoff et al. (2008)). Unlike N_{200}, our richness measurement does not depend on redshift, so we can not make the same correction. However, other sources of variation in the conversion from richness to mass could result in a non-trivial comparison. This may explain our higher redshift L_X at a given Ngal, even when self-similarity predicts the opposite. Another reason for seeing lower X-ray luminosities at higher z is the stellar mass bias present in this population. The DXsC population is pre-selected based on Ngal and is sub-luminous compared to the clusters that would be detected in the X-ray but not in the optical.

While we see slightly different slopes and intercepts for the fits at different redshifts, the overlap is significant. The lack of strong dependence of the L_X-Ngal relation on redshift has several interpretations. The first is that our sample does not have enough data to accurately measure this, especially as low richness. Additional data, which could allow for finer redshift bins and clusters with larger Ngals, would confirm if the lack of z dependence is legitimate or a function of our small sample size. The second is that, since we are selecting clusters using the same technique, the same types of clusters are getting

picked at each redshift, or progenitor bias is occurring. This would ensure that we cannot directly measure the evolution over time. To correct this, we would need to select clusters in a way that would create an evolutionary sequence. This would involve creating lower mass cluster bins at high z and increasing the mass cutoff in the lower z bins. This technique would also require a larger number of clusters in our sample.

4.4 Caveats

Several sources of error could potentially result in different results with our data. One such source of error is the offset between the BCG position and the X-ray peak position. As previously discussed, this is more likely to occur in clusters that have recently undergone a merger, are dynamically un-relaxed, or have BCG positions associated with proto-stellar masses in clusters that are still forming (Webb et al. (2015)). This source of error is tightly connected with clusters with unusual morphologies that reside at high z. We see this in our $S_{3,fianl}$ stack (figure 3.13) and the bootstrap results for that population, which has a much larger spread in L_X than the other stacks. Therefore, the greater agreement we see with the $S_{3,fianl}$ population with DXsC population in figure 3.20 is difficult to trust. We would need additional and higher resolution X-ray data to resolve this issue and confirm if higher z X-ray undetected clusters are more likely to be directly described by the L_X- Ngal relation than X-ray undetected clusters at lower redshift.

Another solution to this issue, which would also improve results in the PCA and bootstrap analysis, is to have a larger sample of optically selected clusters. This would allow for binning in richness in addition to redshift, which would further ensure that the cluster

population going into each stack is homogeneous in central brightness and morphology. The stacks resulting from binning in additional dimensions would demonstrate less spatial variability in their EOFs (figure 3.11). We also note that without the ability to stack in richness space in our stacks, the average X-ray luminosities calculated for each stack may not represent the underlying population. We address this using the bootstrapping analysis and the probability distributions to display the L_X values instead of using only the average value of the stack. This limitation is again a function of the number of clusters in our sample.

4.5 Future work

As previously discussed, the confirmation of many of our results depends on a larger sample size of clusters. This is challenging, as we require a sample of optically selected clusters up to $z \sim 2$ on the order of several thousand. The hyper suprime-cam (HSC) has a wide-field optical imaging survey that is already being used to compare optical clusters to X-ray (Ota et al. (2023)). However, the redshift range of this survey is still limited to $z \sim 1$. We need the Roman Space Telescope to further push the optical data into the NIR regime and to obtain higher z optically selected clusters (Eifler et al. (2021)). With a larger sample, we could create more bins for stacking in the X-ray. The number of stacks created in this analysis were restricted as fewer clusters in each stack resulted in a low SNR and non-significant X-ray flux. Creating stacks at different richnesses in addition to redshifts would allow us to examine the redshift evolution of the L_X-Ngal relation established by X-ray undetected clusters in addition to the detected clusters.

In addition to more optical data, using eROSITA X-ray data instead of *XMM-Newton* will result in the classification of more X-ray counterparts for optically selected clusters, improved resolution, and greater depth. While the eROSITA All-Sky Survey (eRASS) covers the three fields used in this analysis, only one out of eight passes are currently available. The flux limit of the first data release is 5×10^{-14} erg s^{-1} cm^{-2} for the 0.5-2.0 keV energy band, which is similar or worse to the X-ray data used in this work (Ramos-Ceja and the eSASS team). However, when the complete survey comes out, the deeper X-ray data combined with stacking analysis will allow us to examine cluster populations at low richnesses and fainter X-ray luminosities.

Chapter 5

Final Conclusion and summary

In this thesis, we have motivated the need to compare multiple detection methods when studying galaxy clusters. We also motivated the importance of fine-tuning galaxy cluster scaling relations and evaluating their evolution with redshift. We examined the X-ray properties of galaxy clusters in the SpARCS survey which are selected using optical techniques up to $z \sim 2$. We used stacking analysis to increase the exposure time in the X-ray and detect extended X-ray emission from the ICM, which allowed us to measure an average X-ray luminosity for a population of previously un-detected clusters. We used source matching and low-count statistics to identify which SpARCS clusters are also detected in the X-ray, allowing us to compare properties of clusters detectable at different wavelengths. Principal component analysis was used to examine the spatial variance within our stacks and aided in forming a more homogeneous sample. By measuring the surface brightness of the X-ray flux maps created by our stacks, we were able to extract an X-ray luminosity by integrating under a β-model fit to our data. We used bootstrapping to understand further the spread of L_X and Ngal in each stack.

Using the directly and indirectly measured L_X along with the optical richness (Ngal) value assigned to every cluster in the SpARCS survey, we were able to establish an L_X-Ngal scaling relation for X-ray detected and undetected cluster populations.

Our main results are as follows:

- Our sample of undetected X-ray clusters had a large range of morphologies and dynamical states, especially at $z > 1.1$. PCA is an extremely useful tool for examining this limitation when conducting stacking analysis.
- Across all redshifts, we see the population of undetected X-ray SpARCS clusters sitting on the lower end of the X-ray luminosities for a given richness in the L_X-Ngal relation compared to the detected X-ray clusters but still within the scatter.
- Cluster surveys conducted solely using X-ray selection are biased towards clusters with high L_X. Additional detection methods are required to examine the lower L_X clusters at the same redshift and richness.
- There is minimal z evolution in our L_X-Ngal relation. However, this could be due to progenitor bias and a result of all clusters in our sample being chosen in the same way.

A much larger sample of optically selected clusters spanning to high redshift is required to confirm many of our findings. Next-generation facilities will provide the necessary data to continue examining galaxy clusters and their observational biases.

Bibliography

George O. Abell, Jr. Corwin, Harold G., and Ronald P. Olowin. A Catalog of Rich Clusters of Galaxies. , 70:1, May 1989. doi: 10.1086/191333.

Steven W. Allen, August E. Evrard, and Adam B. Mantz. Cosmological parameters from observations of galaxy clusters. *Annual Review of Astronomy and Astrophysics*, 49(1):409–470, sep 2011. doi: 10.1146/annurev-astro-081710-102514.

Michael E. Anderson, Massimo Gaspari, Simon D. M. White, Wenting Wang, and Xinyu Dai. Unifying X-ray scaling relations from galaxies to clusters. *Monthly Notices of the Royal Astronomical Society*, 449(4):3806–3826, April 2015. ISSN 0035-8711. doi: 10.1093/mnras/stv437.

M. Arnaud. The β-model of the intracluster medium. Commentary on: Cavaliere A. and Fusco-Femiano R., 1976, A&A, 49, 137. , 500(1):103–104, June 2009. doi: 10.1051/0004-6361/200912150.

H Bjornsson and SA Venegas. A manual for eof and svd analyses of climatic data. *CCGCR Report*, 97(1):112–134, 1997.

H. Böhringer, P. Schuecker, L. Guzzo, C. A. Collins, W. Voges, R. G. Cruddace, A. Ortiz-Gil, G. Chincarini, S. De Grandi, A. C. Edge, H. T. MacGillivray, D. M. Neumann, S. Schindler, and P. Shaver. The ROSAT-ESO Flux Limited X-ray (REFLEX) Galaxy cluster survey. V. The cluster catalogue. , 425:367–383, October 2004. doi: 10.1051/0004-6361:20034484.

H. Böhringer, K. Dolag, and G. Chon. Modelling self-similar appearance of galaxy clusters in X-rays. , 539:A120, March 2012. doi: 10.1051/0004-6361/201118000.

S. Borgani, F. Governato, J. Wadsley, N. Menci, P. Tozzi, T. Quinn, J. Stadel, and G. Lake. The effect of non-gravitational gas heating in groups and clusters of galaxies. *Monthly Notices of the Royal Astronomical Society*, 336(2):409–424, October 2002. ISSN 0035-8711. doi: 10.1046/j.1365-8711.2002.05746.x.

Richard G. Bower, J. R. Lucey, and Richard S. Ellis. Precision photometry of early-type galaxies in the Coma and Virgo clusters : a test of the universality of the colour-magnitude relation - I. The data. , 254:589–600, February 1992. doi: 10.1093/mnras/254.4.589.

Esra Bulbul, Ang Liu, Thomas Pasini, Johan Comparat, Duy Hoang, Matthias Klein, Vittorio Ghirardini, Mara Salvato, Andrea Merloni, Riccardo Seppi, Julien Wolf, Scott F. Anderson, Y. Emre Bahar, Marcella Brusa, Marcus Brueggen, Johannes Buchner, Tom Dwelly, Hector Ibarra-Medel, Jacob Ider Chitham, Teng Liu, Kirpal Nandra, Miriam E. Ramos-Ceja, Jeremy S. Sanders, and Yue Shen. The eROSITA Final Equatorial-Depth

Survey (eFEDS): Galaxy Clusters and Groups in Disguise. October 2021. arXiv: 2110.09544.

E. T. Byram, T. A. Chubb, and H. Friedman. Cosmic x-ray sources, galactic and extra-galactic. *Science*, 152(3718):66–71, 1966. doi: 10.1126/science.152.3718.66.

C.-T. J. Chen, W. N. Brandt, B. Luo, P. Ranalli, G. Yang, D. M. Alexander, F. E. Bauer, D. D. Kelson, M. Lacy, K. Nyland, P. Tozzi, F. Vito, M. Cirasuolo, R. Gilli, M. J. Jarvis, B. D. Lehmer, M. Paolillo, D. P. Schneider, O. Shemmer, I. Smail, M. Sun, M. Tanaka, M. Vaccari, C. Vignali, Y. Q. Xue, M. Banerji, K. E. Chow, B. Häußler, R. P. Norris, J. D. Silverman, and J. R. Trump. The XMM-SERVS survey: new XMM-Newton point-source catalog for the XMM-LSS field. *Monthly Notices of the Royal Astronomical Society*, 478(2): 2132–2163, August 2018. ISSN 0035-8711, 1365-2966. doi: 10.1093/mnras/sty1036.

L. Chiappetti, M. Pierre, C. Adami, A. Butler, P. Ciliegi, V. Guglielmo, C. Horellou, C. Lidman, A. B. Mantz, M. Ricci, V. Smolcic, Z. Abdulla, R. Adam, S. W. Allen, S. Alis, B. Altieri, S. Arnouts, I. Baldry, N. Baran, C. Benoist, M. Birkinshaw, M. Bolzonella, M. Bondi, A. Bongiorno, D. Bottini, M. Bremer, M. Brown, A. Cappi, C. A. Caretta, J. E. Carlstrom, O. Cucciati, J. Delhaize, S. Desai, S. Driver, D. Eckert, E. Elmer, A. Elyiv, S. Ettori, A. E. Evrard, L. Faccioli, C. Ferrari, S. Fotopoulou, P. Franzetti, B. Garilli, F. Gastaldello, P. Giles, B. Granett, M. Grootes, L. Guennou, L. Guzzo, A. Hopkins, M. Huynh, H. T. Intema, A. Iovino, N. Jurlin, A. Kapinska, F. Karlsson, K. Kolokythas, E. Koulouridis, C. Krook, J. P. Lefevre, J. Liske, H. A. Logan, K. Malek, D. P. Marrone, F. Marulli, B. J. Maughan, S. Maurogordato, S. McGee, O. Melnyk, D. Milakovic, R. Norris, M. Novak, A. Nilsson, A. O'Brien, M. Owers, F. Pacaud, S. Paltani, M. Plionis, B. M.

Poggianti, M. Polletta, A. Pollo, E. Pompei, T. Ponman, M. E. Ramos-Ceja, D. Rapetti, S. Raychaudhury, A. Robotham, H. J. A. Roettgering, T. Sadibekova, M. Scodeggio, M. Sereno, B. Slaus, C. Tasse, L. Tasca, L. Tolliner, R. Tuffs, I. Valtchanov, D. Vergani, C. Vignali, B. Vulcani, G. Wagner, W. Williams, J. Willis, and Consortium The Xxl. VizieR Online Data Catalog: XXL Survey. DR2 (Chiappetti+, 2018). *VizieR Online Data Catalog*, art. IX/52, September 2018.

J. D. Cohn, A. E. Evrard, M. White, D. Croton, and E. Ellingson. Red-sequence cluster finding in the Millennium Simulation. , 382(4):1738–1750, December 2007. doi: 10.1111/j.1365-2966.2007.12479.x.

M. Costanzi, E. Rozo, E. S. Rykoff, A. Farahi, T. Jeltema, A. E. Evrard, A. Mantz, D. Gruen, R. Mandelbaum, J. DeRose, T. McClintock, T. N. Varga, Y. Zhang, J. Weller, R. H. Wechsler, and M. Aguena. Modelling projection effects in optically selected cluster catalogues. , 482(1):490–505, January 2019. doi: 10.1093/mnras/sty2665.

Xinyu Dai, Christopher S. Kochanek, and Nicholas D. Morgan. The x-ray properties of optically selected galaxy clusters. *The Astrophysical Journal*, 658(2):917, apr 2007. doi: 10.1086/509651.

G. B. Dalton, S. J. Maddox, W. J. Sutherland, and G. Efstathiou. The APM Galaxy Survey - V. Catalogues of galaxy clusters. , 289(2):263–284, August 1997. doi: 10.1093/mnras/289.2.263.

I. De Martino and F. Atrio-Barandela. SZ/X-ray scaling relations using X-ray data and Planck Nominal maps. , 461(3):3222–3232, September 2016a. doi: 10.1093/mnras/stw1493.

I. De Martino and F. Atrio-Barandela. SZ/X-ray scaling relations using X-ray data and Planck Nominal maps. , 461(3):3222–3232, September 2016b. doi: 10.1093/mnras/stw1493.

Dominique Eckert, Alexis Finoguenov, Vittorio Ghirardini, Sebastian Grandis, Florian Kaefer, Jeremy Sanders, and Miriam Ramos-Ceja. Low-scatter galaxy cluster mass proxies for the eROSITA all-sky survey. *The Open Journal of Astrophysics*, 3:12, September 2020. doi: 10.21105/astro.2009.13944.

Tim Eifler, Hironao Miyatake, Elisabeth Krause, Chen Heinrich, Vivian Miranda, Christopher Hirata, Jiachuan Xu, Shoubaneh Hemmati, Melanie Simet, Peter Capak, Ami Choi, Olivier Doré, Cyrille Doux, Xiao Fang, Rebekah Hounsell, Eric Huff, Hung-Jin Huang, Mike Jarvis, Jeffrey Kruk, Dan Masters, Eduardo Rozo, Dan Scolnic, David N. Spergel, Michael Troxel, Anja von der Linden, Yun Wang, David H. Weinberg, Lukas Wenzl, and Hao-Yi Wu. Cosmology with the Roman Space Telescope - multiprobe strategies. , 507(2):1746–1761, October 2021. doi: 10.1093/mnras/stab1762.

R. R. Gal, R. R. de Carvalho, S. C. Odewahn, S. G. Djorgovski, and V. E. Margoniner. The Northern Sky Optical Cluster Survey. I. Detection of Galaxy Clusters in DPOSS. , 119 (1):12–20, January 2000. doi: 10.1086/301185.

R. R. Gal, P. A. A. Lopes, R. R. de Carvalho, J. L. Kohl-Moreira, H. V. Capelato, and S. G. Djorgovski. The Northern Sky Optical Cluster Survey. III. A Cluster Catalog Covering PI Steradians. , 137(2):2981–2999, February 2009. doi: 10.1088/0004-6256/137/2/2981.

Andrew Gelman and Andreas Buja. Exploratory data analysis for complex models [with discussion, rejoinder]. *Journal of Computational and Graphical Statistics*, 13(4):755–787, 2004. ISSN 10618600.

David G. Gilbank, Richard G. Bower, F. J. Castander, and B. L. Ziegler. Exploring the selection of galaxy clusters and groups: an optical survey for X-ray dark clusters. , 348 (2):551–580, February 2004. doi: 10.1111/j.1365-2966.2004.07335.x.

P. A. Giles, A. K. Romer, R. Wilkinson, A. Bermeo, D. J. Turner, M. Hilton, E. W. Upsdell, P. J. Rooney, S. Bhargava, L. Ebrahimpour, A. Farahi, R. G. Mann, M. Manolopoulou, J. Mayers, C. Vergara, P. T. P. Viana, C. A. Collins, D. Hollowood, T. Jeltema, C. J. Miller, R. C. Nichol, R. Noorali, M. Splettstoesser, and J. P. Stott. The XMM Cluster Survey analysis of the SDSS DR8 redMaPPer catalogue: implications for scatter, selection bias, and isotropy in cluster scaling relations. , 516(3):3878–3899, November 2022. doi: 10.1093/mnras/stac2414.

S. Giodini, L. Lovisari, E. Pointecouteau, S. Ettori, T. H. Reiprich, and H. Hoekstra. Scaling relations for galaxy clusters: Properties and evolution. *Space Science Reviews*, 177(1-4): 247–282, 2013. doi: 10.1007/s11214-013-9994-5.

Michael D. Gladders and H. K. C. Yee. A New Method For Galaxy Cluster Detection. I. The Algorithm. , 120(4):2148–2162, October 2000. doi: 10.1086/301557.

Michael D. Gladders and H. K. C. Yee. The red-sequence cluster survey. i. the survey and cluster catalogs for patches rcs 0926+37 and rcs 1327+29. *The Astrophysical Journal Supplement Series*, 157(1):1, mar 2005. doi: 10.1086/427327.

J. P. Henry, I. M. Gioia, T. Maccacaro, S. L. Morris, J. T. Stocke, and A. Wolter. The Extended Medium Sensitivity Survey Distant Cluster Sample: X-Ray Data and Interpretation of the Luminosity Evolution. , 386:408, February 1992. doi: 10.1086/171027.

J. Patrick Henry, August E. Evrard, Henk Hoekstra, Arif Babul, and Andisheh Mahdavi. The X-Ray Cluster Normalization of the Matter Power Spectrum. , 691(2):1307–1321, February 2009. doi: 10.1088/0004-637X/691/2/1307.

C. Jones and W. Forman. The structure of clusters of galaxies observed with Einstein. , 276:38–55, January 1984. doi: 10.1086/161591.

Nick Kaiser. Evolution and clustering of rich clusters. *Monthly Notices of the Royal Astronomical Society*, 222(2):323–345, September 1986. ISSN 0035-8711. doi: 10.1093/mnras/222.2.323.

Brandon C. Kelly. Some Aspects of Measurement Error in Linear Regression of Astronomical Data. , 665(2):1489–1506, August 2007. doi: 10.1086/519947.

Ralph P. Kraft, David N. Burrows, and John A. Nousek. Determination of Confidence Limits for Experiments with Low Numbers of Counts. , 374:344, June 1991. doi: 10.1086/170124.

Junyao Li, John D. Silverman, Andrea Merloni, Mara Salvato, Johannes Buchner, Andy Goulding, Teng Liu, Riccardo Arcodia, Johan Comparat, Xuheng Ding, Kohei Ichikawa,

Masatoshi Imanishi, Toshihiro Kawaguchi, Lalitwadee Kawinwanichakij, and Yoshiki Toba. The eROSITA Final Equatorial-Depth Survey (eFEDS): Host-galaxy Demographics of X-ray AGNs with Subaru Hyper Suprime-Cam. *arXiv e-prints*, art. arXiv:2302.12438, February 2023. doi: 10.48550/arXiv.2302.12438.

Yen-Ting Lin and Joseph J. Mohr. K-band Properties of Galaxy Clusters and Groups: Brightest Cluster Galaxies and Intracluster Light. , 617(2):879–895, December 2004. doi: 10.1086/425412.

Yen-Ting Lin, Bau-Ching Hsieh, Sheng-Chieh Lin, Masamune Oguri, Kai-Feng Chen, Masayuki Tanaka, I. Non Chiu, Song Huang, Tadayuki Kodama, Alexie Leauthaud, Surhud More, Atsushi J. Nishizawa, Kevin Bundy, Lihwai Lin, and Satoshi Miyazaki. First Results on the Cluster Galaxy Population from the Subaru Hyper Suprime-Cam Survey. III. Brightest Cluster Galaxies, Stellar Mass Distribution, and Active Galaxies. , 851(2):139, December 2017. doi: 10.3847/1538-4357/aa9bf5.

P. A. A. Lopes, R. R. de Carvalho, H. V. Capelato, R. R. Gal, S. G. Djorgovski, R. J. Brunner, S. C. Odewahn, and A. A. Mahabal. X-ray galaxy clusters in nosocs: Substructure and the correlation of optical and x-ray properties. *The Astrophysical Journal*, 648(1):209, sep 2006. doi: 10.1086/505630.

Paulo A. A. Lopes, M. Trevisan, T. F. Laganá, F. Durret, A. L. B. Ribeiro, and S. B. Rembold. Optical substructure and BCG offsets of Sunyaev-Zel'dovich and X-ray-selected galaxy clusters. , 478(4):5473–5490, August 2018. doi: 10.1093/mnras/sty1374.

Piero Madau and Mark Dickinson. Cosmic Star-Formation History. , 52:415–486, August 2014. doi: 10.1146/annurev-astro-081811-125615.

K. Migkas, F. Pacaud, G. Schellenberger, J. Erler, N. T. Nguyen-Dang, T. H. Reiprich, M. E. Ramos-Ceja, and L. Lovisari. Cosmological implications of the anisotropy of ten galaxy cluster scaling relations. *Astronomy Astrophysics*, 649:a151, 2021. doi: 10.1051/0004-6361/202140296.

R. J. Mitchell, J. C. Ives, and J. L. Culhane. The X-ray temperatures of eight clusters of galaxies and their relationship to other cluster properties. *Monthly Notices of the Royal Astronomical Society*, 181(1):25P–32P, November 1977. ISSN 0035-8711. doi: 10.1093/mnras/181.1.25P.

Joseph J. Mohr, Benjamin Mathiesen, and August E. Evrard. Properties of the Intracluster Medium in an Ensemble of Nearby Galaxy Clusters. , 517(2):627–649, June 1999. doi: 10.1086/307227.

Silvano Molendi. The intra-cluster medium. In *AIP Conference Proceedings*. AIP, 2004. doi: 10.1063/1.1718479.

Andrea Morandi, Stefano Ettori, and Lauro Moscardini. X-ray and Sunyaev–Zel'dovich scaling relations in galaxy clusters. *Monthly Notices of the Royal Astronomical Society*, 379: 518–534, July 2007. ISSN 0035-8711. doi: 10.1111/j.1365-2966.2007.11882.x.

Adam Muzzin, Gillian Wilson, Mark Lacy, H. K. C. Yee, and S. A. Stanford. The Evolution of Dusty Star Formation and Stellar Mass Assembly in Clusters: Results from the IRAC

3.6, 4.5, 5.8, and 8.0 μm Cluster Luminosity Functions. , 686(2):966–994, October 2008. doi: 10.1086/591542.

Adam Muzzin, Gillian Wilson, H. K. C. Yee, Henk Hoekstra, David Gilbank, Jason Surace, Mark Lacy, Kris Blindert, Subhabrata Majumdar, Ricardo Demarco, Jonathan P. Gardner, Mike Gladders, and Carol Lonsdale. SPECTROSCOPIC CONFIRMATION OF TWO MASSIVE RED-SEQUENCE-SELECTED GALAXY CLUSTERS AT z 1.2 IN THE SpARCS-NORTH CLUSTER SURVEY. *The Astrophysical Journal*, 698(2):1934–1942, June 2009. ISSN 0004-637X, 1538-4357. doi: 10.1088/0004-637X/698/2/1934.

Q. Ni, W. N. Brandt, C.-T. Chen, B. Luo, K. Nyland, G. Yang, F. Zou, J. Aird, D. M. Alexander, F. E. Bauer, M. Lacy, B. D. Lehmer, L. Mallick, M. Salvato, D. P. Schneider, P. Tozzi, I. Traulsen, M. Vaccari, C. Vignali, F. Vito, Y. Xue, M. Banerji, K. Chow, A. Comastri, A. Del Moro, R. Gilli, J. Mullaney, M. Paolillo, A. Schwope, O. Shemmer, M. Sun, J. D. Timlin, and J. R. Trump. The XMM-SERVS survey: XMM-Newton point-source catalogs for the W-CDF-S and ELAIS-S1 fields. *The Astrophysical Journal Supplement Series*, 256(1):21, September 2021. ISSN 0067-0049, 1538-4365. doi: 10.3847/1538-4365/ac0dc6.

N. Ota, N. T. Nguyen-Dang, I. Mitsuishi, M. Oguri, M. Klein, N. Okabe, M. E. Ramos-Ceja, T. H. Reiprich, F. Pacaud, E. Bulbul, M. Brüggen, A. Liu, K. Migkas, I. Chiu, V. Ghirardini, S. Grandis, Y. T. Lin, H. Miyatake, S. Miyazaki, and J. S. Sanders. The eROSITA Final Equatorial-Depth Survey (eFEDS). X-ray properties of Subaru's optically selected clusters. , 669:A110, January 2023. doi: 10.1051/0004-6361/202244260.

José Pinto Peixoto and Abraham H. Oort. *Physics of Climate*. American Institute of Physics, New York, 1992. ISBN 978-0-88318-711-1 978-0-88318-712-8.

Ying-jie Peng, Simon J. Lilly, Katarina Kovač, Micol Bolzonella, Lucia Pozzetti, Alvio Renzini, Gianni Zamorani, Olivier Ilbert, Christian Knobel, Angela Iovino, Christian Maier, Olga Cucciati, Lidia Tasca, C. Marcella Carollo, John Silverman, Pawel Kampczyk, Loic de Ravel, David Sanders, Nicholas Scoville, Thierry Contini, Vincenzo Mainieri, Marco Scodeggio, Jean-Paul Kneib, Olivier Le Fèvre, Sandro Bardelli, Angela Bongiorno, Karina Caputi, Graziano Coppa, Sylvain de la Torre, Paolo Franzetti, Bianca Garilli, Fabrice Lamareille, Jean-Francois Le Borgne, Vincent Le Brun, Marco Mignoli, Enrique Perez Montero, Roser Pello, Elena Ricciardelli, Masayuki Tanaka, Laurence Tresse, Daniela Vergani, Niraj Welikala, Elena Zucca, Pascal Oesch, Ummi Abbas, Luke Barnes, Rongmon Bordoloi, Dario Bottini, Alberto Cappi, Paolo Cassata, Andrea Cimatti, Marco Fumana, Gunther Hasinger, Anton Koekemoer, Alexei Leauthaud, Dario Maccagni, Christian Marinoni, Henry McCracken, Pierdomenico Memeo, Baptiste Meneux, Preethi Nair, Cristiano Porciani, Valentina Presotto, and Roberto Scaramella. Mass and Environment as Drivers of Galaxy Evolution in SDSS and zCOSMOS and the Origin of the Schechter Function. , 721(1):193–221, September 2010. doi: 10.1088/0004-637X/721/1/193.

B. M. Poggianti and G. Barbaro. Indicators of star formation: 4000 Å break and Balmer lines. , 325:1025–1030, September 1997. doi: 10.48550/arXiv.astro-ph/9703067.

P. Popesso, A. Biviano, E. Bulbul, A. Merloni, J. Comparat, N. Clerc, Z. Igo, A. Liu, S. Driver, M. Salvato, M. Brusa, Y. E. Bahar, N. Malavasi, V. Ghirardini, G. Ponti,

A. Robotham, J. Liske, and S. Grandis. The X-ray invisible Universe. A look into the halos undetected by eROSITA. *arXiv e-prints*, art. arXiv:2302.08405, February 2023. doi: 10.48550/arXiv.2302.08405.

M. E. Ramos-Ceja and MPE the eSASS team. De:futureerassreleases. URL `https://erosita.mpe.mpg.de/erass/`.

A. Rettura, R. Chary, J. Krick, and S. Ettori. Mass–richness relations for x-ray and sze-selected clusters at 0.4 lt; z lt; 2.0 as seen by spitzer at 4.5 m. *The Astrophysical Journal*, 867(1):12, oct 2018. doi: 10.3847/1538-4357/aad818.

Piero Rosati, Stefano Borgani, and Colin Norman. The Evolution of X-ray Clusters of Galaxies. , 40:539–577, January 2002. doi: 10.1146/annurev.astro.40.120401.150547.

M. Rossetti, F. Gastaldello, D. Eckert, M. Della Torre, G. Pantiri, P. Cazzoletti, and S. Molendi. The cool-core state of Planck SZ-selected clusters versus X-ray-selected samples: evidence for cool-core bias. , 468(2):1917–1930, June 2017. doi: 10.1093/mnras/stx493.

E. Rozo, J. G. Bartlett, A. E. Evrard, and E. S. Rykoff. Closing the loop: a self-consistent model of optical, X-ray and Sunyaev-Zel'dovich scaling relations for clusters of Galaxies. , 438(1):78–96, February 2014. doi: 10.1093/mnras/stt2161.

E. S. Rykoff, T. A. McKay, M. R. Becker, A. Evrard, D. E. Johnston, B. P. Koester, E. Rozo, E. S. Sheldon, and R. H. Wechsler. Measuring the Mean and Scatter of the X-Ray Luminosity–Optical Richness Relation for maxBCG Galaxy Clusters. *The Astrophysical Journal*, 675(2):1106–1124, March 2008. ISSN 0004-637X, 1538-4357. doi: 10.1086/527537.

C. A. Scharf, H. Ebeling, E. Perlman, M. Malkan, and G. Wegner. The wide-angle rosat pointed x-ray survey of galaxies, groups, and clusters. i. method and first results. *The Astrophysical Journal*, 477(1):79, mar 1997. doi: 10.1086/303698.

N. Scoville, S. Arnouts, H. Aussel, A. Benson, A. Bongiorno, K. Bundy, M. A. A. Calvo, P. Capak, M. Carollo, F. Civano, J. Dunlop, M. Elvis, A. Faisst, A. Finoguenov, Hai Fu, M. Giavalisco, Q. Guo, O. Ilbert, A. Iovino, M. Kajisawa, J. Kartaltepe, A. Leauthaud, O. Le Fèvre, E. LeFloch, S. J. Lilly, C. T. C. Liu, S. Manohar, R. Massey, D. Masters, H. J. McCracken, B. Mobasher, Y. J. Peng, A. Renzini, J. Rhodes, M. Salvato, D. B. Sanders, B. D. Sarvestani, C. Scarlata, E. Schinnerer, K. Sheth, P. L. Shopbell, V. Smolčić, Y. Taniguchi, J. E. Taylor, S. D. M. White, and L. Yan. Evolution of Galaxies and Their Environments at z = 0.1-3 in COSMOS. , 206(1):3, May 2013. doi: 10.1088/0067-0049/206/1/3.

Tomomi Sunayama, Youngsoo Park, Masahiro Takada, Yosuke Kobayashi, Takahiro Nishimichi, Toshiki Kurita, Surhud More, Masamune Oguri, and Ken Osato. The impact of projection effects on cluster observables: stacked lensing and projected clustering. , 496(4):4468–4487, August 2020. doi: 10.1093/mnras/staa1646.

R. A. Sunyaev and Ya. B. Zeldovich. The Observations of Relic Radiation as a Test of the Nature of X-Ray Radiation from the Clusters of Galaxies. *Comments on Astrophysics and Space Physics*, 4:173, November 1972.

E. W. Upsdell, P. A. Giles, A. K. Romer, R. Wilkinson, D. J. Turner, M. Hilton, E. Rykoff, A. Farahi, S. Bhargava, T. Jeltema, M. Klein, A. Bermeo, C. A. Collins, L. Ebrahimpour,

D. Hollowood, R. G. Mann, M. Manolopoulou, C. J. Miller, P. J. Rooney, Martin Sahlén, J. P. Stott, P. T. P. Viana, S. Allam, O. Alves, D. Bacon, E. Bertin, S. Bocquet, D. Brooks, D. L. Burke, M. Carrasco Kind, J. Carretero, M. Costanzi, L. N. da Costa, M. E. S. Pereira, J. De Vicente, S. Desai, H. T. Diehl, J. P. Dietrich, S. Everett, I. Ferrero, J. Frieman, J. García-Bellido, D. W. Gerdes, G. Gutierrez, S. R. Hinton, K. Honscheid, D. J. James, K. Kuehn, N. Kuropatkin, M. Lima, J. L. Marshall, J. Mena-Fernández, F. Menanteau, R. Miquel, J. J. Mohr, R. L. C. Ogando, A. Pieres, M. Raveri, M. Rodriguez-Monroy, E. Sanchez, V. Scarpine, I. Sevilla-Noarbe, M. Smith, E. Suchyta, M. E. C. Swanson, G. Tarle, C. To, N. Weaverdyck, J. Weller, and P. Wiseman. The XMM cluster survey: exploring scaling relations and completeness of the dark energy survey year 3 redMaPPer cluster catalogue. , 522(4):5267–5290, July 2023. doi: 10.1093/mnras/stad1220.

G. Mark Voit. Tracing cosmic evolution with clusters of galaxies. *Reviews of Modern Physics*, 77(1):207–258, April 2005. doi: 10.1103/RevModPhys.77.207.

Michael L. Waskom. seaborn: statistical data visualization. *Journal of Open Source Software*, 6(60):3021, 2021. doi: 10.21105/joss.03021.

Tracy M. A. Webb, Adam Muzzin, Allison Noble, Nina Bonaventura, James Geach, Yashar Hezaveh, Chris Lidman, Gillian Wilson, H. K. C. Yee, Jason Surace, and David Shupe. The Star Formation History of BCGs to z = 1.8 from the SpARCS/SWIRE Survey: Evidence for Significant In Situ Star Formation at High Redshift. , 814(2):96, December 2015. doi: 10.1088/0004-637X/814/2/96.

J. P. Willis, M. E. Ramos-Ceja, A. Muzzin, F. Pacaud, H. K. C. Yee, and G. Wilson. X-ray versus infrared selection of distant galaxy clusters: a case study using the XMM-LSS and SpARCS cluster samples. , 477(4):5517–5535, July 2018. doi: 10.1093/mnras/sty975.

Gillian Wilson, Adam Muzzin, H. K. C. Yee, Mark Lacy, Jason Surace, David Gilbank, Kris Blindert, Henk Hoekstra, Subhabrata Majumdar, Ricardo Demarco, Jonathan P. Gardner, Michael D. Gladders, and Carol Lonsdale. SPECTROSCOPIC CONFIRMATION OF A MASSIVE RED-SEQUENCE-SELECTED GALAXY CLUSTER AT z = 1.34 IN THE SpARCS-SOUTH CLUSTER SURVEY. *The Astrophysical Journal*, 698(2):1943–1950, June 2009. ISSN 0004-637X, 1538-4357. doi: 10.1088/0004-637X/698/2/1943.